



Anatomic and Functional Imaging using Row-Column Arrays

Jensen, Jørgen Arendt; Schou, Mikkel; Jørgensen, Lasse Thurmand; Tomov, Borislav G.; Stuart, Matthias Bo; Traberg, Marie Sand; Taghavi, Iman; Øygard, Sigrid Husebø ; Ommen, Martin Lind; Steenberg, Kitty

Total number of authors:
14

Published in:
IEEE Transactions on Ultrasonics, Ferroelectrics, and Frequency Control

Link to article, DOI:
[10.1109/TUFFC.2022.3191391](https://doi.org/10.1109/TUFFC.2022.3191391)

Publication date:
2022

Document Version
Peer reviewed version

[Link back to DTU Orbit](#)

Citation (APA):

Jensen, J. A., Schou, M., Jørgensen, L. T., Tomov, B. G., Stuart, M. B., Traberg, M. S., Taghavi, I., Øygard, S. H., Ommen, M. L., Steenberg, K., Thomsen, E. V., Panduro, N. S., Nielsen, M. B., & Sørensen, C. M. (2022). Anatomic and Functional Imaging using Row-Column Arrays. *IEEE Transactions on Ultrasonics, Ferroelectrics, and Frequency Control*, 69(10), 2722-2738. Article 9830770. <https://doi.org/10.1109/TUFFC.2022.3191391>

General rights

Copyright and moral rights for the publications made accessible in the public portal are retained by the authors and/or other copyright owners and it is a condition of accessing publications that users recognise and abide by the legal requirements associated with these rights.

- Users may download and print one copy of any publication from the public portal for the purpose of private study or research.
- You may not further distribute the material or use it for any profit-making activity or commercial gain
- You may freely distribute the URL identifying the publication in the public portal

If you believe that this document breaches copyright please contact us providing details, and we will remove access to the work immediately and investigate your claim.

Anatomic and Functional Imaging using Row-Column Arrays

Jørgen Arendt Jensen¹, Mikkel Schou, Lasse Thurmand Jørgensen¹, Borislav G. Tomov¹, Matthias Bo Stuart¹, Marie Sand Traberg¹, Iman Taghavi¹, Sigrid Huesebø Øygaard¹, Martin Lind Ommen², Kitty Steenberg², Erik Vilain Thomsen², Nathalie Sarup Panduro³, Michael Bachmann Nielsen⁴ and Charlotte Mehlin Sørensen³

¹Center for Fast Ultrasound Imaging, ²MEMS Group, Dept. of Health Technology, Technical University of Denmark, DK-2800 Lyngby, Denmark,

³Dept. of Biomedical Sciences, University of Copenhagen, DK-2100 Copenhagen, Denmark,

⁴Dept. of Radiology, Rigshospitalet, Copenhagen, DK-2100 Copenhagen, Denmark

Abstract—Row-column (RC) arrays have the potential to yield full three-dimensional ultrasound imaging with a greatly reduced number of elements compared to fully populated arrays. They, however, have several challenges due to their special geometry. This review paper summarizes the current literature for RC imaging and demonstrate that full anatomic and functional imaging can attain a high quality using synthetic aperture (SA) sequences and modified delay-and-sum beamforming. Resolution can approach the diffraction limit with an isotropic resolution of half a wavelength with low side-lobe levels, and the field-of-view can be expanded by using convex or lensed RC probes. GPU beamforming allows for 3 orthogonal planes to be beamformed at 30 Hz, providing near real time imaging ideal for positioning the probe and improving the operator’s workflow. Functional imaging is also attainable using transverse oscillation and dedicated SA sequence for tensor velocity imaging for revealing the full 3-D velocity vector as a function of spatial position and time for both blood velocity and tissue motion estimation. Using RC arrays with commercial contrast agents can reveal super resolution imaging with isotropic resolution below 20 μm . RC arrays can, thus, yield full 3-D imaging at high resolution, contrast, and volumetric rates for both anatomic and functional imaging with the same number of receive channels as current commercial 1-D arrays.

I. INTRODUCTION

Currently 2-D ultrasound imaging is mostly conducted using 1-D array transducers with 192 to 256 elements, which are employed to dynamically focus the image. Digital beamformers are used, where the signal from each transducer element is sampled at 4 to 8 times the center frequency for sampling rates between 12 to 60 MHz. A fully populated 15 MHz array with 256 channels will, thus, give data rates up to 30.7 GBytes per second, which are beamformed in real time. Currently most arrays have a fixed geometric focus in the elevation plane (orthogonal to the imaging plane), and the focusing is often poor in this direction, underlining the necessity for 3-D focusing and imaging.

Attaining 3-D ultrasound images requires electronic steering in both the azimuth and elevation directions to allow dynamic focusing along all three directions (axial, azimuth and elevation). Matrix array were early conceived as they allow full control in both directions in both transmit and receive.



Fig. 1: Fully populated matrix array from Philips with beamforming in the handle. The probe has 9,212 active elements, but note that the plug can only handle 256 simultaneous connections.

However, it creates another practical problem as the number of channels increase quadratically with the side-length of the array assuming a square array aperture. A straight forward translation to 3-D would give arrays with $192 \times 192 = 36,864$ elements or $256 \times 256 = 65,536$ elements yielding data rates of 2,560 GBytes/s, which is clearly not possible to process in real time. This has been solved by making sparse matrix probes, where only part of the elements are connected resulting in higher side lobe levels [1–6]. A second approach is to make micro-beamforming in the handle to reduce the amount of data. Philips has introduced the fully-sampled matrix phased array x-Matrix probe shown in Fig. 1 with 9,212 elements, which potentially could have 96×96 elements. Such a probe can be steered in both directions, and this necessitates an element size of half a wavelength λ given by

$$\lambda = c/f_0, \quad (1)$$

where c is the speed of sound (1540 m/s in tissue) and f_0 is the transducer center frequency. In this case for a 3 MHz probe the element size is $250 \mu\text{m}$ and the side length of the probe is $48\lambda = 24 \text{ mm}$. Much of the beamforming is performed in the transducer handle to reduce the amount of data coming out of the probe to probably 256 channels, making this an extremely complex and expensive probe to develop and manufacture.

The focusing ability of ultrasound probes is related to their size and the imaging depth. The Full-Width-Half-Max (FWHM) of the point spread function is:

$$\text{FWHM} = \lambda F\# = \lambda \frac{D}{W}, \quad (2)$$

where D is the imaging depth and W is the aperture width, and $F\#$ is the F-number, where its lowest theoretical value is $1/2$ (the diffraction limit). The best possible attainable lateral resolution is, thus, $\lambda/2$. For the Philips probe this can only be attained down to 12 mm, and after 48 mm the resolution goes beyond 2λ , which is considered as the resolution limit for an acceptable ultrasound image. In cardiology a lower resolution has to be accepted due to the narrow space between the ribs, which prevents the use of larger probes when scanning the heart. In other applications with a wider acoustic window, such resolution is not acceptable.

In other clinical specialties the matrix probe should be larger, further increasing the amount of elements and the complexity of the probes. In general, the lateral resolution in the two planes scales with the side length of the probe, and increasing the resolution by two will quadruple the number of probe elements. Matrix probes are, thus, not an optimal approach for attaining a high image quality, and conventional 1-D array probes have a poor out-of-plane resolution limiting their ability to visualize small objects, when they are not at the elevation focus. Other solutions for optimal imaging are therefore needed.

A. History of row-column imaging

A possible solution to these problems is to employ row-column (RC) array probes [7–25]. Here, the matrix elements are addressed as either rows or columns as shown in Fig. 2. The amount of connections to a $N \times N$ elements array is $2N$, reducing the amount of connections by $N/2$, which for a 256×256 elements arrays is a factor of 128. Often, only rows or columns are used in transmit and the orthogonal elements in receive, and suitable multiplexing can therefore reduce the scanner connection to N , a further reduction by 2.

It is, thus, possible to have very large RC arrays without the amount of connections to the array getting prohibitively large. The consequence of this is a theoretical focusing capability, which is much better than for a fully populated array, as the width of the array is larger, and the FWHM is correspondingly smaller.

The area of the array scales quadratically with the side length or element count, which is beneficial for the transmitted pressure and the received energy. RC probes can therefore have an increased penetration depth compared to other probes as demonstrated in [26].

The initial idea of RC arrays was presented by Lockwood's group at Queen's University, Canada in [7] with simulations of a convex array for revealing the imaging area and point spread function. Further simulations were given in [17]. Fabrication of such an array and data from its use was given in [27].

The group by Yen at the University of Southern California, USA has also fabricated a number of arrays and extensively investigated their performance. Initial simulations of a 256×256

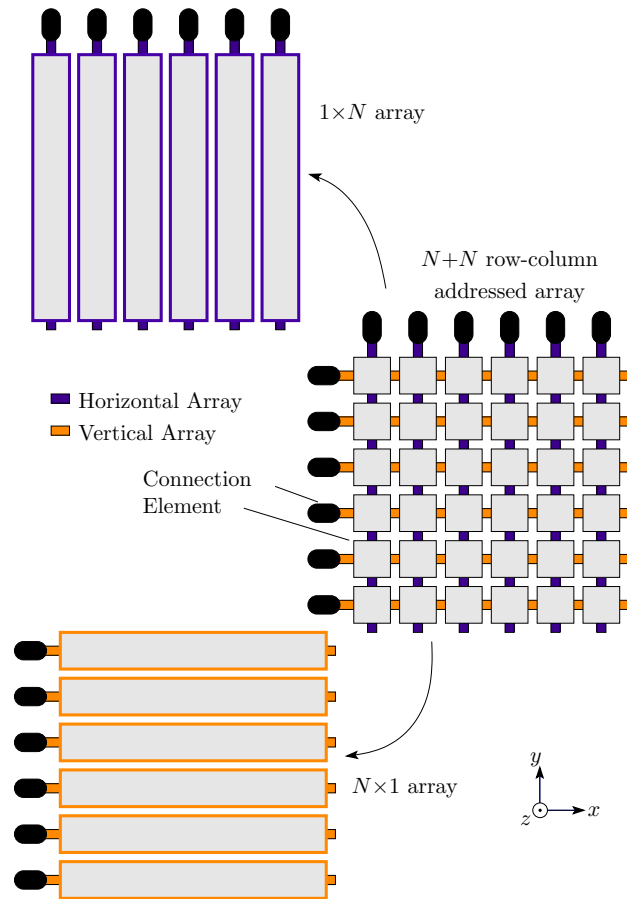


Fig. 2: A row-column-addressed 2-D transducer array can be interpreted as two orthogonal 1-D arrays. To the right is shown a 2-D transducer array, where each transducer element is addressed by its row or column index, effectively creating the two arrays shown to the left (from [24]).

row-column array were presented in [8] with more extensive simulations in [9]. Results from a 64×64 PZT array operating at 5.6 MHz were shown in [10] and later for an impressive 256×256 PZT array operating at 6.4 MHz with a size of 40×40 mm [12]. More results from a cyst phantom were presented in [13] and a full overview of the results are given in [16]. A spatial compounding method for row-column arrays used on the a 256×256 PZT array is described in [14]. Examples of a 32×32 elements CMUT array with a center frequency of 5.45 MHz along with another 32×32 elements array operating at center frequency of 12 MHz were presented in [15, 18], showing that high frequency and high bandwidth row-column arrays can be fabricated in CMUT technology.

A novel approach similar to row-column arrays for 3-D imaging was presented by the group at Roma Tre University, Italy using the concept of a criss-cross array [11], where a CMUT array with two spatially superimposed linear orthogonal arrays was investigated. This yields $2N$ connections and an imaging example using two emissions to reduce grating lobes were presented. A fabricated CMUT prototype with overlapping arrays was presented in [28] with $120 + 120$ elements, and imaging was conducted using the ULA-OP

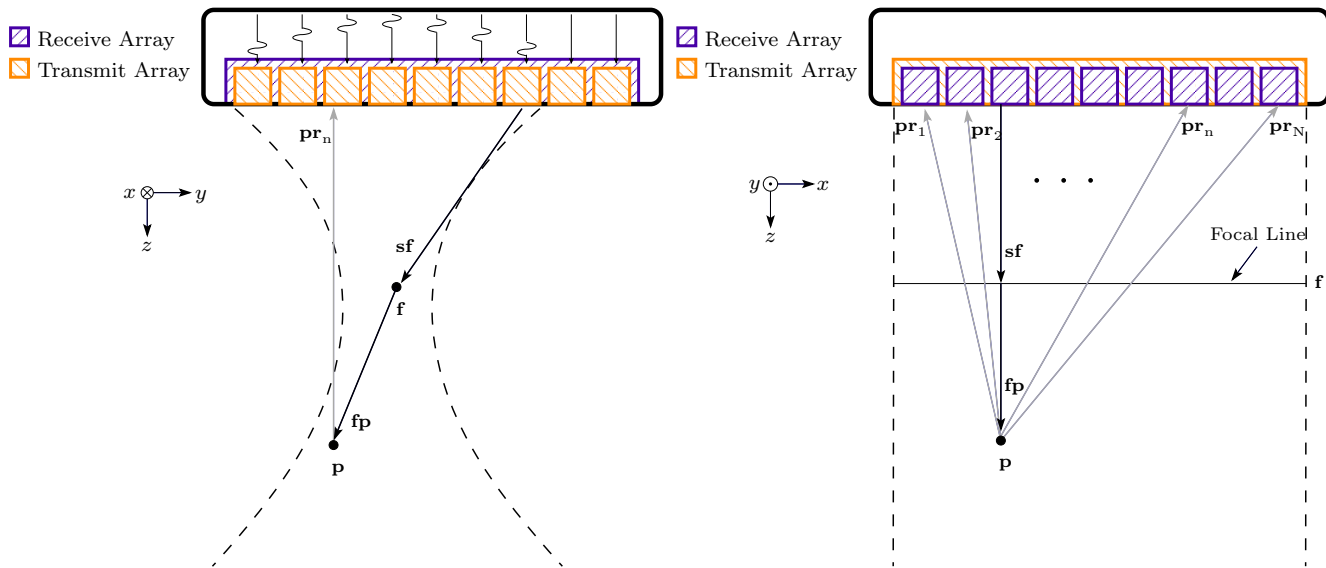


Fig. 3: Time of flight (ToF) illustration of a focused emission. The vector \mathbf{sf} connects the first source line element that is excited with the focal line \mathbf{f} . \mathbf{fp} is the vector from the nearest point on the focal line to the point being beamformed (\mathbf{p}), and \mathbf{pr}_n is the vector from \mathbf{p} to the nearest point on the receive line element \mathbf{r}_i . On the left figure, the setup is sliced orthogonal to the transmitting line elements and parallel with the receiving line elements. On the right figure, the setup is sliced parallel with the transmitting line elements and orthogonal to the receiving line elements. The focal zone \mathbf{f} on the left looks like a focal point, but on the right it is seen to be a focal line (text and figure from [24]).

scanner [29]. Focusing in the orthogonal plane was attained by approximating a Fresnel lens using a varying bias voltage across elements.

The Zemp group at the University of Alberta, Canada has also developed a series of RC probes often under the name TOBE: Top-Orthogonal-to-Bottom Electrode. The feasibility and fabrication of such an array was presented in [30] for a 64×64 elements array fabricated in CMUT technology with more details in [23]. Its use for photo-acoustic imaging was demonstrated in [31] using a laser for excitation and synthetic aperture imaging for creating the image. Chee and Zemp described an advanced modulation scheme in [32], where a combination of individual elements could be acquired simultaneously for the CMUT TOBE array. Other combinations of this scheme were presented in [33] and [34], and results with side lobes below 45 dB were attained. Recent results for a 10 MHz 64×64 elements electrostrictive array using Hadamard encoding in transmit for an increased signal-to-noise ratio and synthetic aperture focusing were presented in [35] and for a 30 MHz in [36], demonstrating the good image quality of these arrays and imaging schemes.

The Tanter group at the Institut Langevin, Paris, France has also worked extensively with row-column arrays, especially for flow estimation and super resolution imaging. A plane wave compounding scheme was described in [37] and used for Power Doppler imaging (detecting the presence of flow). Using that scheme for flow imaging has unfortunately revealed fairly high grating lobes [38]. The approach has also been used for imaging a rat brain in [39, 40] using a 15 MHz 128×128 PZT array.

Our group in Denmark has worked extensively with RC arrays for the last ten years within anatomic and functional

imaging primarily based on synthetic aperture (SA) sequences. We have also fabricated a range of RC probes including PZT and CMUT based devices [41] and developed fabrication schemes for diverging lenses and probes with integrated lenses [42, 43]. The various results and possibilities will be presented below. The challenges of using RC array are detailed in Section II, and the possibilities for making anatomic images are shown in Section III, and blood velocity estimation is presented in Section V. A method for super resolution image is presented in Section VI, and a discussion of the benefits, challenges, and future potential are presented in the concluding Section VII.

II. CHALLENGES FOR ROW-COLUMN IMAGING

RC arrays have a number of challenges, which have to be addressed before high quality imaging can be performed. As for all ultrasound imaging schemes, data can be acquired in principally two different ways: focused emissions or broad insonation of the region of interest. The first option will, for 3-D imaging, give an unacceptably low volume rate, unless multiple lines are beamformed in receive as in the early approaches to volumetric imaging [44, 45]. The second approach broadly insonates the volume of interest using cylindrical or plane waves, which decouples frame rate and number of image lines. Examples of such imaging will be given in Section III.

A second challenge is the large elements. In ordinary imaging the elements can be considered point sources and delay-and-sum beamforming is employed based on the geometric distance from emissions through the imaging point to the receiving element. For a row-column array the elements are large, and this changes the emitted field and the calculation

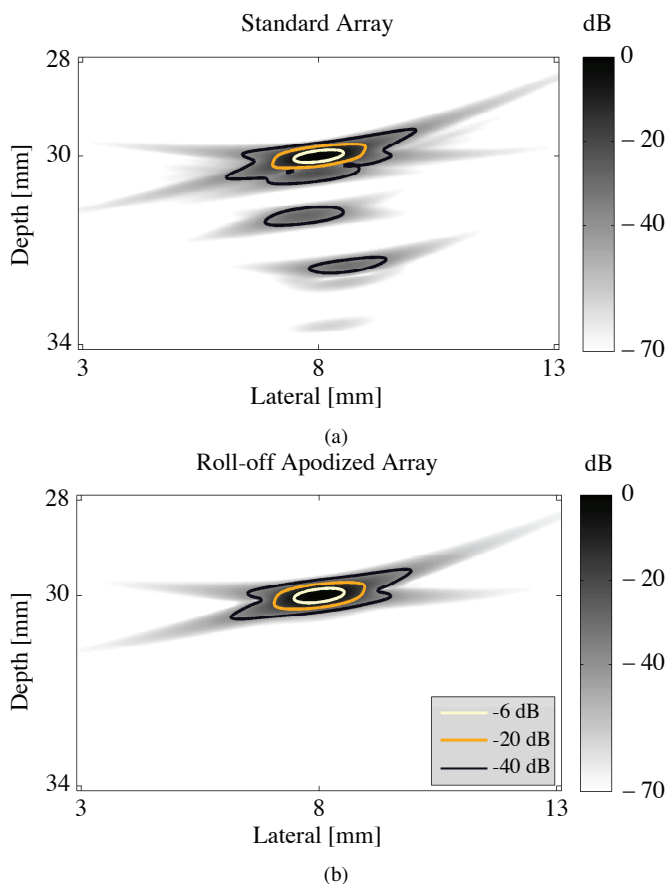


Fig. 4: Point spread function (PSF) for two 64×64 simulated RC arrays at $(x, y, z) = (8, 3, 30)$ mm. The PSF of a standard non-apodized transducer array is shown in (a) and the PSF of a transducer array with integrated roll-off apodization is shown in (b). The main response of the PSFs are practically identical, but the ghost echoes of the roll-off apodized array are greatly suppressed compared to the non-apodized standard array (from [24]).

of delays. The long elements will give rise to an emitted field, which can be considered a plane wave along the length of the element and a circular wave across the element or essentially a cylindrical shaped wave. This should be taken into consideration when predicting the wavefront's position in focusing the image, as is done in the beamformers described in [24]. The focusing calculation in the two orthogonal planes is illustrated in Fig. 3 for the time-of-flight calculation. A precise mathematical description of this can be found in [24].

The large size elements only makes it possible to image in the rectangular region below the probe, and the beam cannot be steered outside this region for pulse-echo imaging. How to solve this problem is described in Section IV-B on lensed and convex RC arrays.

A third challenge from the long elements is the edge waves generated at the ends of the element. The long elements will delay these edge waves significantly compared to the main wave, and this leads to ghost echos after the main point spread function as shown in Fig. 4. The top image show the point spread function for a 62×62 elements array, where

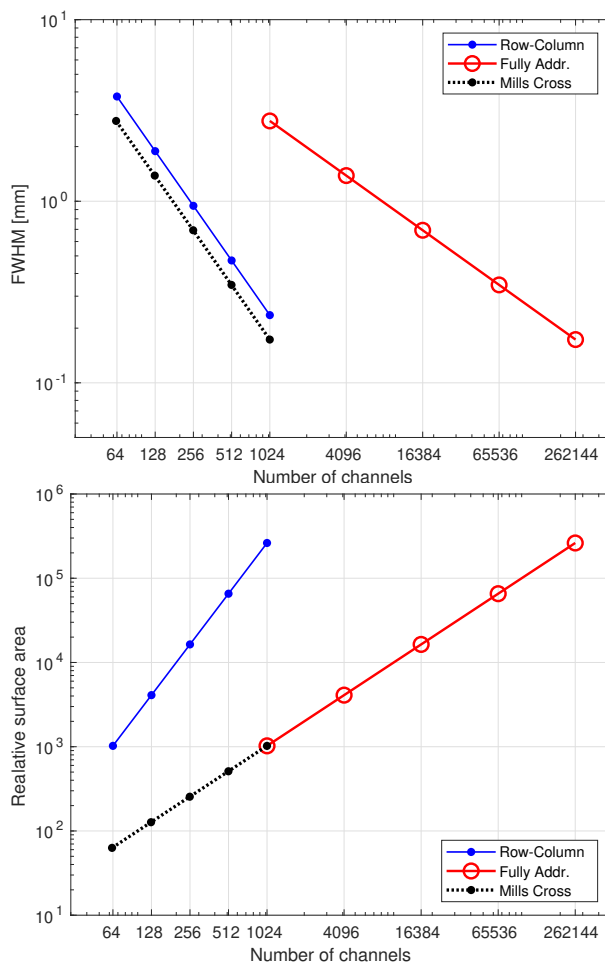


Fig. 5: Comparison of resolution (top) and array size (bottom) between a RC, a fully populated and the Mills cross array (from [26]).

edge echos are seen after the main response. This can be avoided by introducing a roll-off apodization at the edge of the elements to taper off their end response and reduce edge artifacts. This has been employed on the bottom figure, where the ghost echos disappear.

The major benefit of the RC arrays is of course their size, which benefits their focusing ability and penetration depth. This is illustrated in Fig. 5, where they are compared to both fully populated arrays and sparse Mills-cross arrays [46]. The area, corresponding to penetration depth, is always larger for RC arrays and the side length is the same as for the most sparse 2-D array, yielding a comparable FWHM resolution. The RC arrays, thus, attain both a good penetration depth and a narrow focus.

RC arrays, however, have several issues to address to attain high quality imaging including that the contrast of the images are often slightly lower than for current 2-D scanners. These issues are described in the following Sections, starting with the general principles of synthetic aperture imaging, which is needed to attain an optimal image quality and a high volume imaging rate.

III. ANATOMIC IMAGING

Row-column arrays can be used in two fundamentally different ways: using focused emissions or using synthetic aperture (SA) imaging with circular or plane emissions. The first necessitates that the image lines are acquired one at a time, and for a volume with 100×100 lines this often takes more than a second. The preferred method is therefore to use SA imaging, where dynamic transmit focusing is attained by emitting with a number of broadly insonifying beams and by receiving with the orthogonal array elements for dynamic receive focusing. Emitting with waves that are plane in both directions and tilted along the steerable direction, also called ultrafast imaging, has been studied in [37, 38] and [47], which, however, seems to give fairly high side- and grating lobes.

The second wave type is circular waves, which are plane along the long direction of the transmit element and circular in the orthogonal direction. These virtual sources can have a negative F-number for a diverging wave, or they can be focused for increasing the transmitted pressure. Both focus placements seek to acquire data suitable for creating a synthetic transmit aperture. Synthetic transmit aperture imaging can be used for improving the image quality by having dynamic focusing in both transmit and receive [48]. The imaging is performed by circular transmission with a single or a collection of elements. The origo of the wave is therefore known precisely and can be used in the beamformation. The scattered signal is then received by all elements of the orthogonal transducer elements. The path from transmission to reception can, thus, be precisely calculated. A full volumetric image of the object is focused for each emission as the whole image volume is insonified. This is a low resolution volume, as it is only focused in transmit. Repeating the process for a number of virtual sources and summing all the low resolution volumes will yield a high resolution volume, which is dynamically focused in both transmit and receive.

The spread of the virtual sources and the corresponding largest distance span will determine the FWHM attainable in the transmit direction and correspondingly, the spread of the receive elements will determine the FWHM in the orthogonal direction. The contrast for the resulting point spread function (PSF) is determined by the number of transmit sources and the number of receiving elements. Currently, the best image quality is attained by emitting with a virtual source in one direction and then receiving with the orthogonal elements. SA focusing will then yield the optimal PSF, if the beamformer described in Section IV-A is employed. Often a group of elements is used as emitters to increase the emitted energy [49, 50], and the effective width of the aperture is then reduced by the number of elements in the virtual source.

The focusing ability is also dependent on how many receiving element that can contribute to the receive focusing, which is determined by the acceptance angle given by [51]:

$$\alpha = 2 \arctan \frac{1}{2F\#}$$

A wide element will restrict the acceptance angle and increase the possible F-number. The minimum attainable F-number of 0.5 is obtained when the element has a size of half a

wavelength. This also applies for the transmitting elements, and the ideal pitch of the row-column array is, thus, $\lambda/2$.

A. B-mode performance of row-column arrays

An example of the PSF and image quality obtainable from a 6 MHz Vermon 128 x 128 elements RC array is shown in Fig. 6. A SA sequence with 96 row emissions followed by 96 column emissions were made using an F-number of -0.7 with 32 elements and Hanning apodization in transmit. The scattered signals were received on all 128 orthogonal elements. This was beamformed with a F-number of 0.7 and a Hanning apodization for both transmit and receive. Imaging was conducted on a 3-D printed point spread function (PSF) phantom [52] with scattering cavities in a $6 \times 4 \times 4$ grid with a 2.05 mm spacing in all three directions. The scatterers are 205 μm wide along the $x-y$ axes, but only 80 μm in the z direction. A Verasonics Vantage 256 scanner was used for the measurements shown on the top row in Fig. 6, and Field II [53, 54] was used for the corresponding simulation shown in the second row.

An isotropic resolution of $(1.05\lambda, 1.10\lambda, 0.62\lambda) = (x, y, z)$ is attained for the measured data, and a similar performance is seen for the simulated data. The data is also compared to a simulated 6 MHz linear array translated over the aperture in steps of 0.2 mm obtaining 100 images. A 12 emissions SA sequence was used, and the images from this volumetric scanning is seen in the third row. The linear array probe has an elevation resolution determined by the geometric elevation focus at 22 mm with an F-number of 4.4, and the four rows of point scatterers can therefore not be differentiated due to the fixed elevation focus. The acquisition of the linear array data set necessitated $12 \times 100 = 1200$ emissions and mechanical translation, whereas the row-column data set used 192 emissions corresponding to a normal focused linear array image. A volume rate of 52 Hz can therefore be attained down to a depth of 7 cm.

Finally the bottom row in Fig. 6 shows in-vivo images of a Sprague-Dawley rat kidney. The dynamic range is 60 dB and an isotropic speckle pattern is seen in all three imaging planes due to SA imaging, a constant F-number throughout the image, and the large size of the RC array.

Resolution as a function of depth is visualized on the two left columns in Fig. 7, where points are seen in the $x-z$ planes and the wires in the $y-z$ direction. The array has also been used for scanning a tissue mimicking cyst phantom with an attenuation of 0.5 dB/[MHz cm] as shown in the two right most columns in Fig. 7. The cyst size diameters are 2.0, 4.0 and 8.0 mm. The 2 mm cysts can clearly be seen down to 50 mm, and the 4 and 8 mm cysts are visible down to the penetration depth of 110 mm.

The array used here is far from optimal for SA imaging. No edge apodization is included in the array and the probe pitch is λ , which limits the acceptance angle in both transmit and receive. An optimal array with both these properties does currently not exist, and can therefore only be simulated. The optimal resolution possible using SA imaging for a 192×192 elements RC array has been simulated for two types of

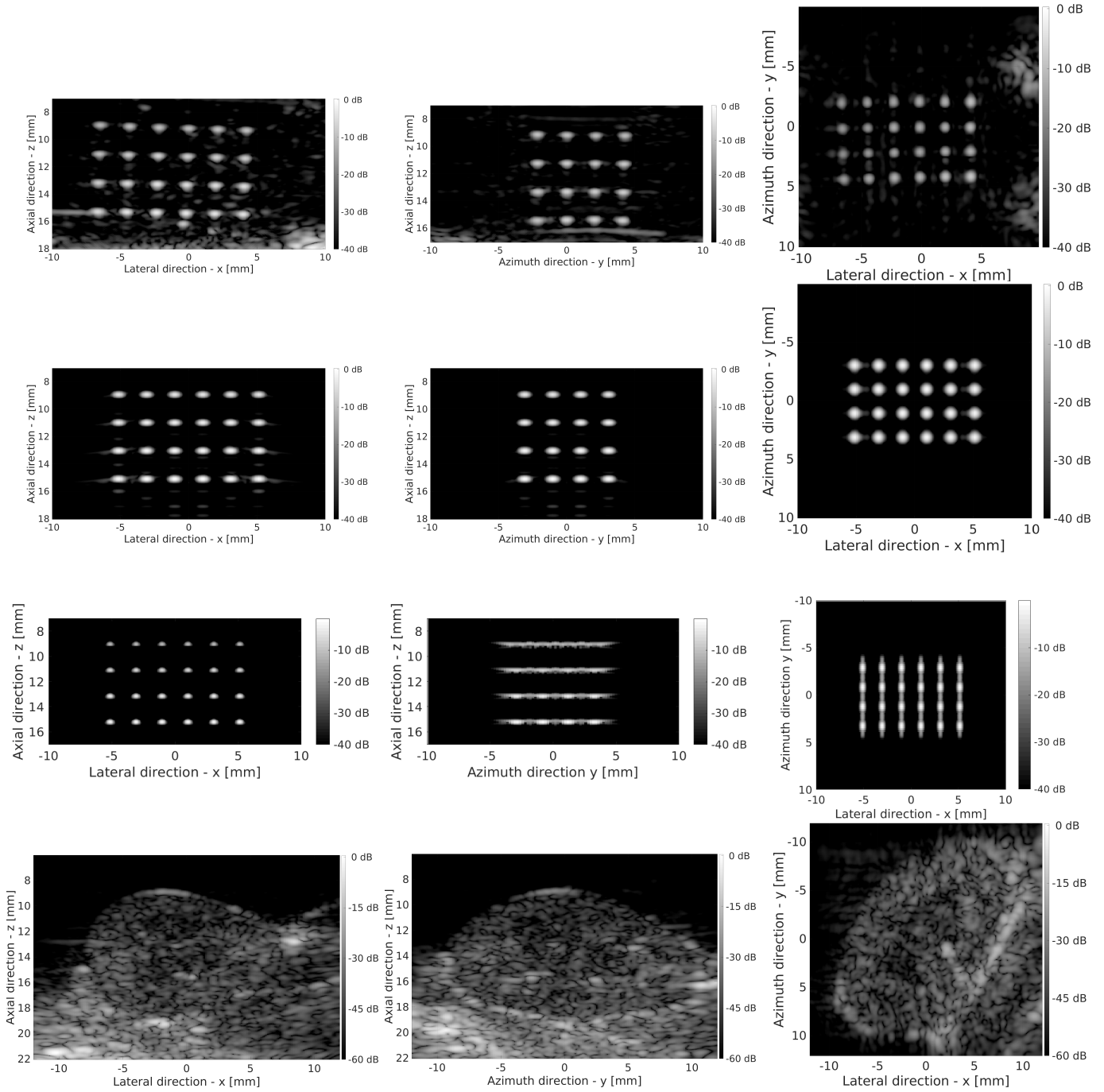


Fig. 6: Point spread functions obtained from a 3-D printed phantom with isolated point targets using a 6 MHz Vermon 128 x 128 elements row-column array with λ pitch. The top row shows the measured images in the $x-z$, $y-z$ and $y-x$ planes (left to right). The corresponding simulated data from the phantoms is shown in the next row. Simulated data for a linear array probe translated across the phantom is shown in the next row for a GE 6 MHz linear array using a SA sequence. The bottom row shows images of a rat kidney in all three planes.

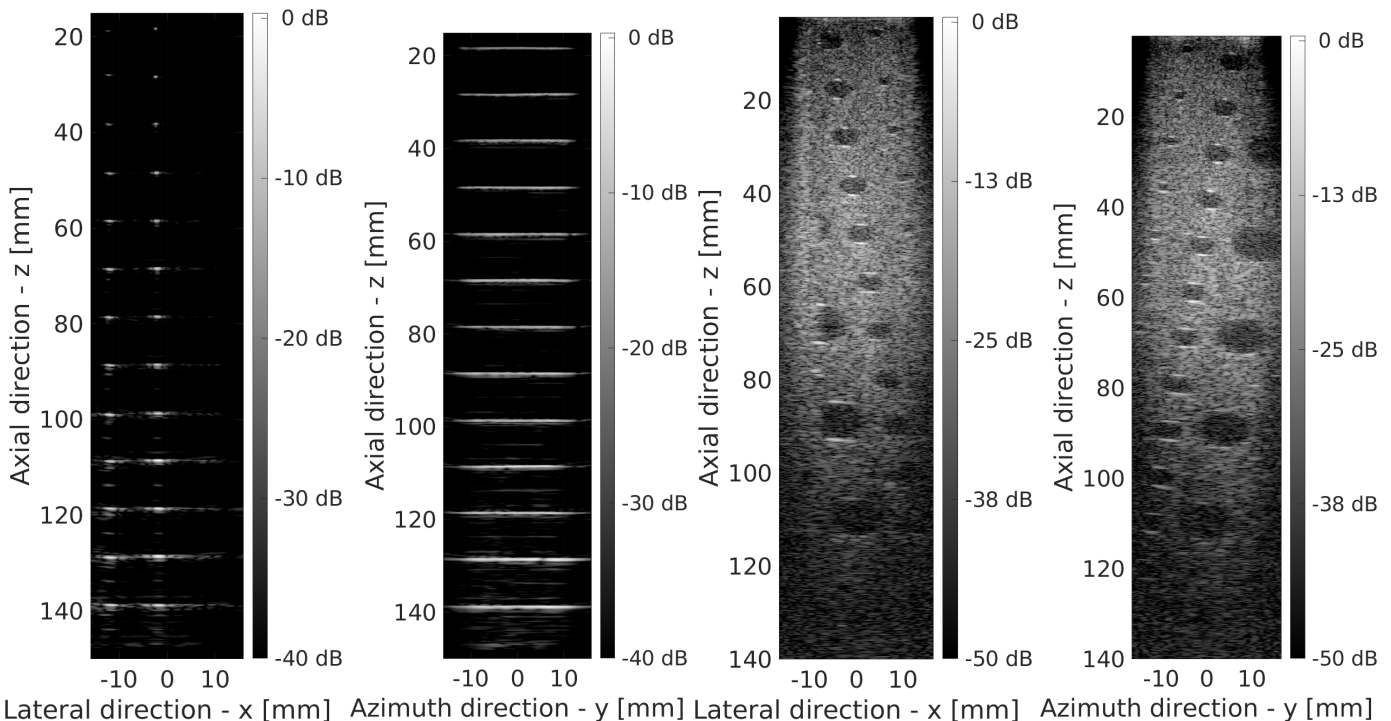


Fig. 7: Two left columns: Orthogonal wire phantom images for the Vermont RC probe for a matrix wire phantom with two rows of wires stretch out along the y -direction. Two right columns: Orthogonal cyst phantom images for the Vermont RC probe for a tissue mimicking phantom with an acoustical attenuation of $0.5 \text{ dB}/[\text{MHz cm}]$.

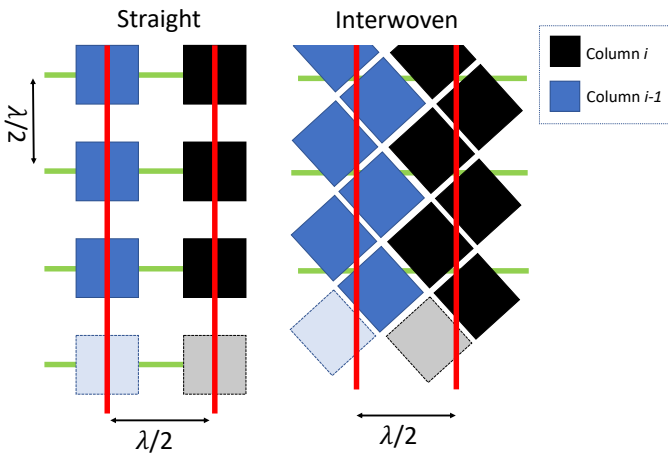


Fig. 8: Simulation setup. To the left, the straight element RC array is visualized. The cells have $\lambda/2$ spacing, which matches the inter-element spacing. The interwoven structure is visualized to the right. The red lines symbolize the assumed acoustic center of the column elements, the green likewise for the rows (from [55]).

arrays in [55]. Both have $\lambda/2$ pitch for optimal imaging with geometries shown in Fig. 8, where the first is a traditional rectangular grid array and the other is an interwoven array for increasing the active area of the array. The second array is only possible to manufacture with silicon CMUT fabrication

TABLE I: Estimated metrics for the simulated PSFs for the two 192×192 elements RCAs (from [55]).

| FWHM | Azimuth-Range | Elevation - Range | C-plane |
|---------------|----------------|-------------------|----------------|
| Straight | 0.62λ | 0.60λ | 0.60λ |
| Interwoven | 0.61λ | 0.62λ | 0.62λ |
| CR20dB | Azimuth-Range | Elevation-Range | C-plane |
| Straight | 1.42λ | 1.42λ | 1.43λ |
| Interwoven | 1.34λ | 1.34λ | 1.30λ |

processes, whereas the first array can be made using traditional PZT technology. The long elements are edge apodized to avoid the ghost artifacts after the point spread functions. Imaging is conducted by emitting with one element at a time and receiving with the orthogonal elements, so a full volume uses 192 emissions, which is the same as for normal linear array imaging, but here the full volume is acquired and perfectly focused in all three directions.

The point spread functions for the arrays were simulated in Field II and the quantitative numbers for FWHM and contrast are shown in Table I. It can be seen that the resolution is very close to ideal obtainable resolution of $\lambda/2$ for SA focusing and a good contrast is also obtained. Full apodization in transmit and receive has not been employed, and that is why the PSFs are not round and have edge effect artifact, which can be avoided with proper apodization. The contrast is slightly lower than for normal SA imaging 1-D arrays, due to the switching between rows and columns in transmit and receive.

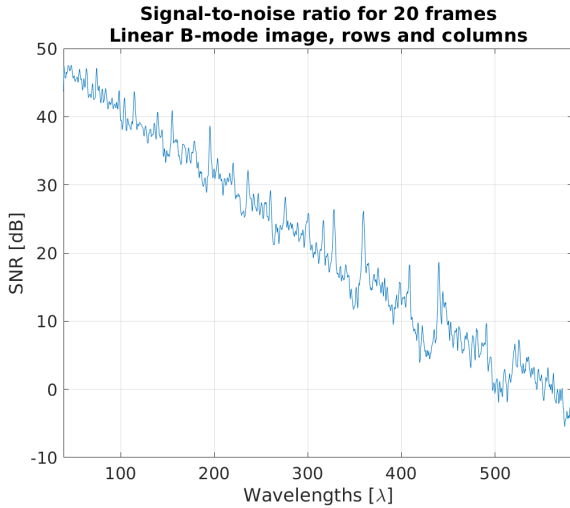


Fig. 9: SNR of the Vermont RC probe for a tissue mimicking phantom with an acoustical attenuation of 0.5 dB/[MHz cm] for the images shown in Fig. 7. The wavelength λ for soft tissue is 0.257 mm for the 6 MHz probe, and 400λ corresponds to 102.7 mm. The penetration depth when the SNR is 0 dB is roughly 550λ corresponding to 141 mm.

IV. IMAGING PENETRATION FOR ROW-COLUMN ARRAYS

The large active area of the row-column probe is advantageous for attaining a large penetration depth, defined as the imaging depth, where the signal-to-noise ratio attains a value of 0 dB. This is shown in Fig. 9, where the 128×128 elements Vermont RC array was used for imaging a cyst phantom with an attenuation of 0.5 dB/[MHz cm]. The 6 MHz PZT array attains a penetration down to 11 cm or 428λ when using only 32 elements in transmit using an F-number of -1. Similar results have been attained in [26] for two 62×62 elements RC arrays, one fabricated using CMUT technology and one traditional PZT array. The 3 MHz PZT array attained a penetration down to 14 cm when using only a single element in transmit, whereas using an F-number of 1 or -1 gave predicted penetration depths of 25 to 30 cm, considerably more than the conventional array's penetration of 300 to 400λ (15-20 cm). Here it should also be kept in mind that these are first version prototype arrays, the experimental scanner SARUS [56] was used, and the arrays were fairly small (62×62 elements, $\lambda/2$ pitch). A more realistic array with 256×256 elements would have a 16 times larger surface area, and using a better prototype and scanner would also significantly increase the penetration depth. This can be translated to imaging with a higher center frequency, if the large penetration depth is not needed, which would increase resolution in all three directions proportionally to the wavelength. For the 62×62 elements PZT probe using an F-number of -1 the measured mechanical index MI was 0.67 and the derated spatial-peak-temporal average intensity I_{spta} was 0.53 mW/cm. The allowable limits for MI is 1.9 and 720 mW/cm for I_{spta} for peripheral vessels [57]. It is, thus, possible also to increase the transmitted pressure by a factor 3, and the limit on I_{spta} can essentially not be reached, showing the further potential for increasing

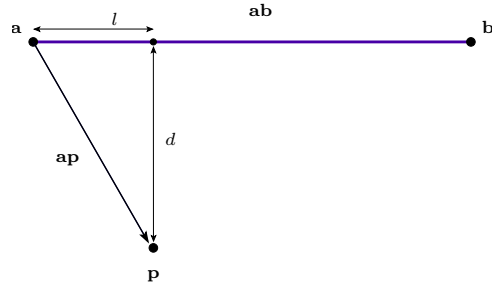


Fig. 10: Projection of the point \mathbf{p} onto the line segment \mathbf{ab} . l is the distance from \mathbf{a} to the projected point and d is the shortest distance from \mathbf{p} to \mathbf{ab} (from [24]).

the signal-to-noise ratio.

A. Beamforming implementations

Beamforming of row-column data must take into account the long and narrow elements, where the emitted field is a plane wave along the long side and a circular wave in the orthogonal direction as shown in Fig. 3. The left figure illustrates a focused emission at \mathbf{sf} in the $y-z$ plane and the emission of the plane wave in the $x-z$ plane, so the emitted field is described as a focal line and not as a focal point. The time-of-flight calculation has to take this into account, where the transmit time is from the transducer surface to the focal line and from the focal line to the field point \mathbf{fp} . The time to reception is then from \mathbf{fp} to the center of the receiving elements. The projection of the distances to the long elements is shown in Fig. 10. A more detailed explanation and the exact equations can be found in [24].

The importance of replacing the delay calculation with the specifics for the row-column array rather than the traditional spherical delay calculation is illustrated in Fig. 11, where the received signal quickly attains the wrong geometric position, if the new calculation method is not employed. This can both lead to the geometric distortion shown, but also leads to a diminished resolution and contrast, if not implemented properly.

Efficient implementations of this type of beamforming has been developed for a GPU in [58, 59]. The software is written under the CUDA environment and takes in radio frequency (RF) data from the row-column channels and then yields a focused line, image, or volume. The beamformer is parametric and can be used for very large volumes only limited by the RAM of the GPU card. An example of performance for a state-of-the-art Titan V Nvidia card is shown in Fig. 12. This roughly corresponds to the newer Nvidia GTX 3090 card. This GPU can attain a beamforming performance of around 40 Gsamples per second. Two intersecting B-mode images with 96 lines containing 512 samples for a 192×192 elements row-column array can, thus, be beamformed with a frame rate around 30 Hz, when 64 emissions are used for creating the volume. A full volume with 96×96 lines can be beamformed in 1.45 seconds. It is, thus, possible to make real time scanning

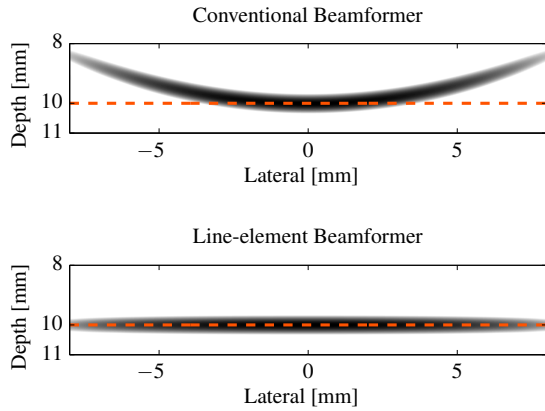


Fig. 11: B-mode images of a wire phantom beamformed with a conventional beamformer (top) and with the proposed line element beamformer (bottom). The dashed lines indicate the location of the wire phantom. The B-mode images are shown with a dynamic range of 40 dB. When using a conventional beamformer, the B-mode is seen to be geometrically distorted (from [24]).

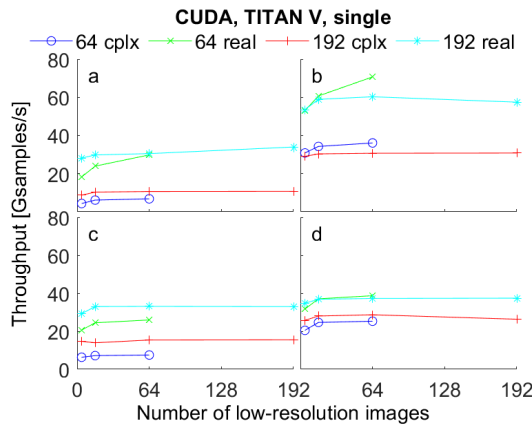


Fig. 12: Throughput as function of number of low resolution images for the CUDA beamformer on the TITAN V GPU with single precision calculations. (a) and (b) show through-puts for the shallow phantom, and (c) and (d) show for the deep phantom. (a) and (c) show for cross planes, and (b) and (d) show for full volumes. The colored lines show performance for 64 or 192 receiving elements and for real or complex (cplx) sample values (from [58]).

and plane visualization with a state-of-the-art GPU card, and the full volume can be beamformed in a reasonable time for off-line visualization and inspection.

B. Lensed row-column imaging

Currently, flat row-column probes can only image in the rectilinear region below the active transducer surface. This is acceptable for small parts imaging near the probe surface, but for abdominal or cardiac imaging the field of view is too limited and has to be expanded. This can be attained

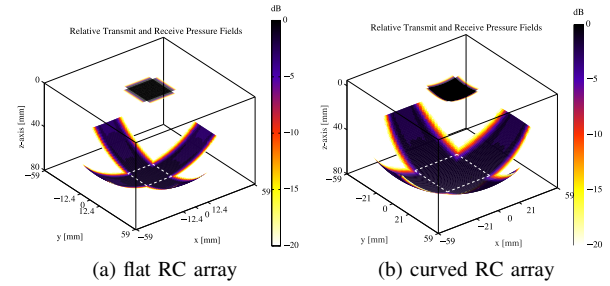


Fig. 13: Relative transmit and receive pressure fields at radial distance of 80 mm for azimuth and elevation steering angles from -45° to 45° . The imaging area is the intersection of these two fields, which is (a) the rectilinear forward-looking box, and (b) the curvilinear forward-looking region in front of the transducer using a lens with $f_\# = -1$ (from [60]).

using either a lens in front of the probe or by fabricating a convex probe. The imaging region is illustrated in Fig. 13 for both a flat and a lensed array, which expands the usable field-of-view. The flat array is restricted by the large elements, which limits the field along the element length, and the combination of transmitting with e.g. the rows and receiving with the orthogonal elements gives a field-of-view, which is the intersection of the two limited regions. This is expanded by the diverging lens, as shown in the right figure.

Lensed row-column probes are in the early stage of development, and very few results have so far been published [60, 61]. The results are based on concave lenses attached to the 62×62 element probe described before [24, 25], and it is needed to modify the beamforming geometry to include this in the delay calculations. Fig. 14 illustrates how the diverging lens changes the time-of-flight, and that has to be accounted for in the beamformer as described in [60].

The diverging lens beamformer has been simulated for both point and cyst phantoms with good results demonstrating the larger field-of-view. The same general trend is seen for the cyst phantom simulations, where a larger field-of-view is attained along with a good contrast in the image [60]. Lenses for the 62×62 elements row-column array have been fabricated and tested on the arrays. Results for wire and cyst phantoms have been measured and processed and are shown in Figs. 15 and 16. They both show similar results as for the simulations that an increased field-of-view is attained along with good focusing abilities and an acceptable contrast. More results and details can be found in [61].

The current equations in the lensed beamformer give reasonable results, but it has been shown that ray tracing theory can further enhance the quality of the results and increase the field-of-view [62]. This should be further investigated and incorporated in the beamformers.

C. Convex row-column imaging

An obvious method to avoid making a lens would be to shape the RC probe in a double curved, convex shape as suggested in [17]. The synthetic aperture sequence developed

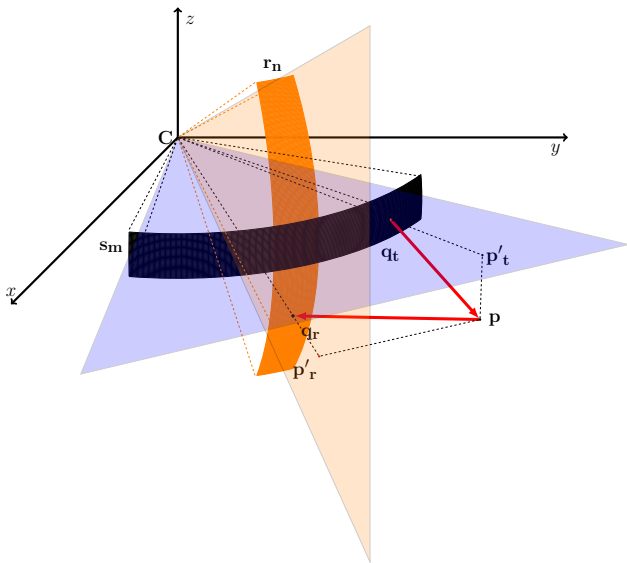


Fig. 14: The time-of-flight of a wavefront is given by the shortest distance from the source s_m to the point being focused p and back to the receiving element r_n , divided by the speed of sound (from [60]).

for flat RC arrays would be nearly directly applicable to a convex array, where the beamforming then would take the geometry into account. Such arrays would have many benefits for abdominal ultrasound imaging. Their foot-print could be made quite large, which ensures a low F-number even for large depths. The large size would also ensure a large penetration depth, as the emitted energy is distributed over a large area keeping MI low but still acquiring the returned energy from a large surface. Démoré et al [17] demonstrated that a 128×128 RC convex array could cover at $60^\circ \times 60^\circ$ sector with a good image quality using their imaging scheme.

V. FLOW IMAGING

Current commercial scanners can all display the velocity of blood in the human circulation. The blood motion is detected by estimating the positional shift between two emissions using correlation-based estimators finding either the phase or the time shift [63]. These methods are well established and widely used in the clinical for quantifying vascular diseases. They, however, have several drawbacks. The detected shift is only in direction of the ultrasound beam, and most vessels run parallel to the skin surface, so the least important velocity component is detected. This is often remedied by titling the ultrasound beam and introducing angle compensation methods. These are unreliable for angles close to 90 degrees and for complicated vessel geometries, the angle will vary as a function of space and time precluding a single angle correction factor. This has been remedied by introducing vector flow imaging (VFI) in a number of methods [64, 65]. One VFI method uses the transverse oscillation approach where an oscillation perpendicular to the ultrasound beam is introduced during receive beamforming, and the shift in the lateral direction can then be estimated yielding the full 2-D velocity vector [66, 67].

This has been shown in a number of clinical studies to give improved flow estimates, which are more consistent and easier to use for medical doctors [68].

A. Tensor velocity imaging

The VFI approach gives consistent results for flow in the 2-D plane, but neglects the out-of-plane component. The approach has therefore been translated to RC arrays for both traditionally focused emissions [69, 70] and for a fast SA based approach [71, 72] using interleaved SA imaging [73, 74]. Here, the full 3-D blood velocity is estimated in the volume for each time instance for full tensor velocity imaging (TVI). The probe can be placed to just cover the vessel, and the full velocity vector is estimated for any position in the volume with hundreds of estimates per second.

An example of tensor velocity imaging is shown in Fig. 17 for measured pulsating flow in a carotid artery phantom, where the arrows indicate direction and the colors indicate the velocity magnitude. The velocities over time for different positions in the vessel are indicated in Fig. 17, showing that the velocity components in all directions can be estimated as a function of time everywhere in the volume. The full 3-D vector velocity field can therefore be acquired for a couple of heart-beats, and the velocity for any place and time can be determined retrospectively after the acquisition has been made, thus, increasing the clinical relevance.

Further validation of the TVI method was performed using finite element (FEM) simulations of pulsating flow in an in-silico carotid artery phantom [75], where the ground truth is known. Motion correction was employed to improve the estimates [72], and the result is shown in Fig. 18 for both an auto-correlation estimator (left column), cross-correlation estimator (middle column), and for the ground truth FEM data. The estimates were found using an f_{prf} of 20 kHz and only 62 receive channels. In general, the relative standard deviation and bias were below 5% in most cases, yielding fully quantitative results independent of the relative position between the vessel and the probe.

VI. SUPER RESOLUTION IMAGING

The latest addition to medical ultrasound is super resolution imaging, where the micro-vasculature can be visualized down to vessel sizes of $20\text{-}50 \mu\text{m}$. This is attained by injecting a standard contrast agent (SonoVue) intravenously and then image the motion of the gas filled bubbles. A sparse distribution of bubbles makes it possible to track individual bubbles and establish their position with micrometer precision [76–82]. The data is acquired over minutes and motion correction of the acquired data must be performed to maintain resolution [83–89], but as most of the current methods are in two dimensions, they cannot compensate for large motions and out-of-plane motion.

It has been demonstrated that row-column probes also can be used for super resolution imaging [90]. A 3 MHz 62×62 elements RC array with a half wavelength pitch was used with a Synthetic Aperture (SA) pulse inversion sequence with 32

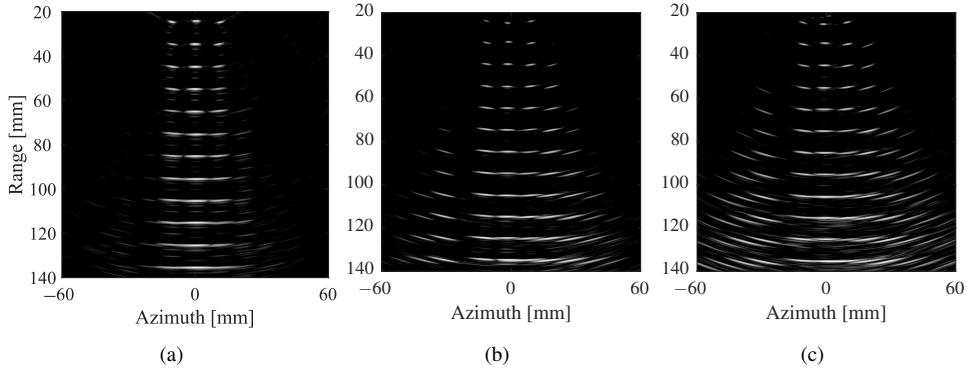


Fig. 15: Examples of a wire grid phantom imaged without and with different lenses are shown using a 30 dB dynamic range, (a) without lens, (b) for the 25.4 mm radius lens, and (c) for the 12.7 mm radius lens (modified from [61]).

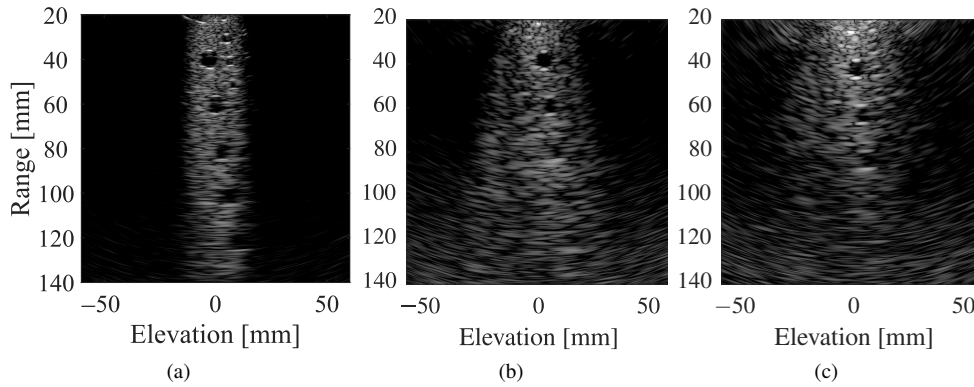


Fig. 16: Hollow cyst phantom images with both lenses are shown using a 40 dB dynamic range, (a) without lens, (b) for the 25.4 mm radius lens, and (c) for the 12.7 mm radius lens (modified from [61]).

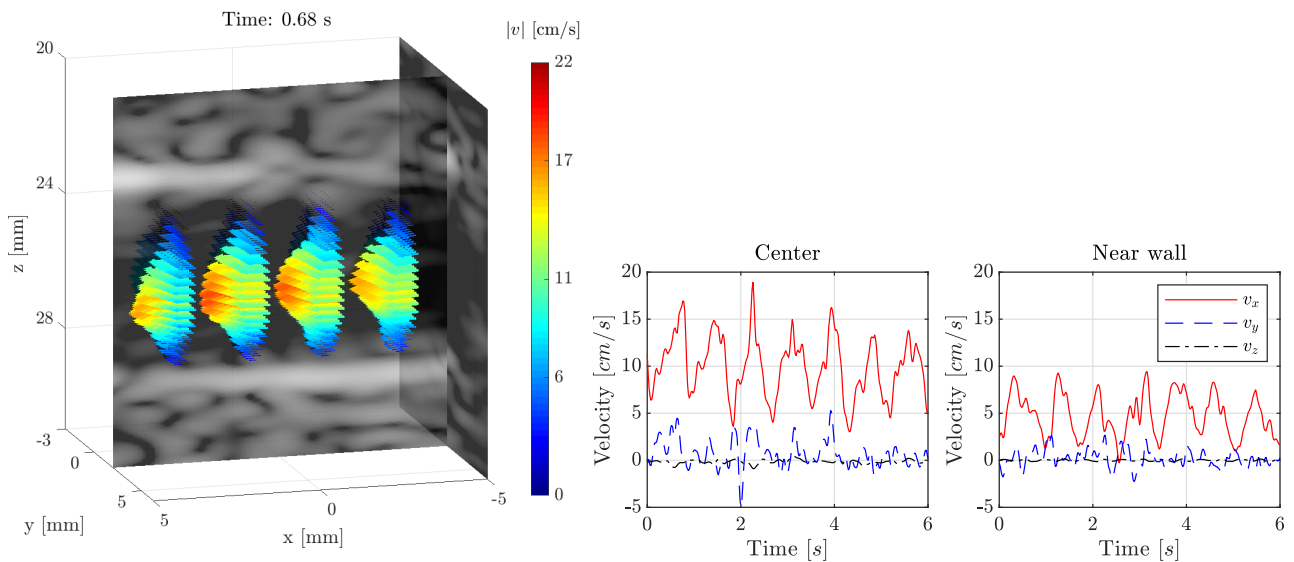


Fig. 17: Pulsating flow in a tissue mimicking phantom is shown on the left. The flow is visualized using arrows, where color shows velocity magnitude and the arrows depict velocity direction and magnitude. The middle graph shows all three velocity components v_x, v_y, v_z (red, blue, black) for a point in the vessel center. The right graph shows the components at a point placed near the vessel wall (modified from [71]).

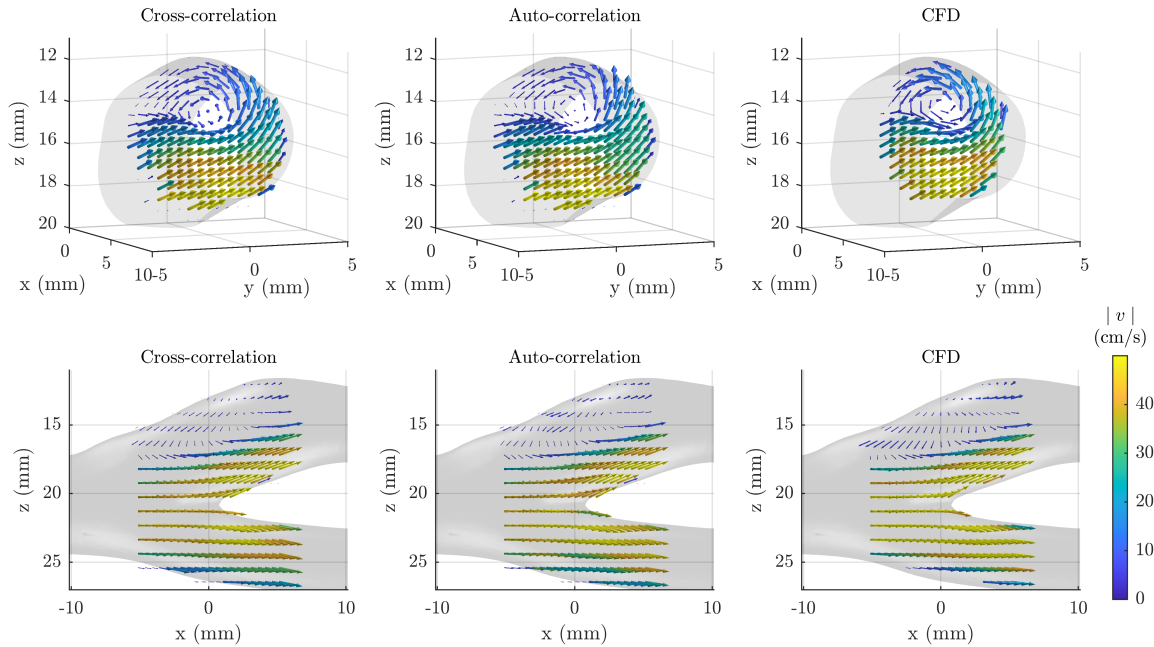


Fig. 18: Tensor velocity imaging using a 62×62 elements RC array from simulated data in the carotid artery for two different estimators compared to the ground truth finite element data on the right. Arrows indicate direction and magnitude, which is also indicated by the color. A vortex in the upper vessel branch is seen in the top row, and reverse flow is also present in the bottom row (from [75]).

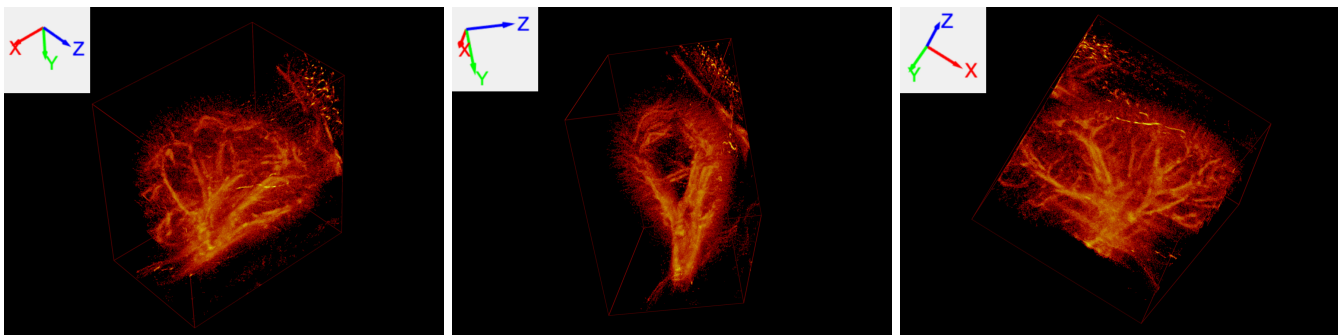


Fig. 19: Super resolution images of the vasculature in a Sprague-Dawley rat kidney acquired in vivo using the 6 MHz 128×128 RC array. SonoVue was injected intravenously and the data acquired over 135 seconds. The images show the large segmental arteries and veins, the smaller arcuate vessels, and the small cortical radial vessels extending towards the surface of the kidney. The B-mode images are shown in Fig. 6.

positive and 32 negative row emissions for acquiring volumetric data using the SARUS research ultrasound scanner. Data received on the 62 columns were beamformed on a GPU for a maximum volume rate of 156 Hz, when the pulse repetition frequency was 10 kHz. Investigations were performed on 3-D printed point and flow micro-phantoms, where the flow micro-phantom contained a $100 \mu\text{m}$ radius tube injected with the contrast agent SonoVue. The 3-D processing pipeline uses the volumetric envelope data to find the bubble's positions from their interpolated maximum signal and yielded a high resolution in all three coordinates. The localization precision for tracking a 3-D printed point phantom was $(20.7, 19.8, 9.1) \mu\text{m}$ in the x, y, z coordinates. The flow micro-phantom had an

estimated radial precision of $16.5 \mu\text{m}$ in the $y-z$ plane, and $23 \mu\text{m}$ in the $x-z$ plane [90].

This approach has been translated to the Vermon 128×128 array for measurements on a Sprague-Dawley rat kidney. An amplitude modulation sequence with 3 emissions for the same virtual source and 48 virtual sources spread out over the row elements was employed at a pulse repetition frequency of 20 kHz between the three emissions and 1.3 kHz between the virtual sources for a volume rate of 24 Hz. A 1:5 dilution of SonoVue at an intravenous infusion rate of $55 \mu\text{l}/\text{min}$ was employed over the 135 s acquisition. The data was then processed with a SRI pipeline as described above, and the final 3-D images are shown in Fig. 19 for three different views.

The volume rate was fairly low, to keep the data rate low to enable acquisition over a long period of time. For this shallow scanning down to 3 cm, f_{prf} could be maintained at 25 kHz for a volume rate of 250 Hz or recursive imaging [91] could be used to raise the volume rate to 8.3 kHz.

This technique makes it possible to visualize the flow in vessels with sizes down to 20 μm , which can be used in the diagnosis of vascular diseases found along with e.g. cancer and diabetes. The images can both reveal the anatomy of the vasculature to reveal vascular rarefaction, neovascularization, increased tortuosity etc. and give quantitative data for the flow to identify changes caused by disease [92, 93].

VII. DISCUSSION AND CONCLUSIONS

It has been shown that RC arrays essentially can be used for any kind of ultrasound imaging for visualizing the anatomy, blood flow, tissue motion, and to perform super resolution imaging allowing visualization of the microvasculature and measurement of flow velocities in the microcirculation. The active number of array elements is of the same order as for conventional 1-D arrays, and the number of transmitters and receivers are therefore as for conventional 2-D imaging. Demands on the transmit stage, receive data rates, and storage sizes are also the same as for 2-D imaging. The number of beamforming operations depends on what should be visualized in terms on planes and volumes, but high-end GPU cards are capable of attaining real-time visualization of orthogonal planes, and 3-D solid volumes can be calculated in seconds [58, 59].

A good B-mode image quality can be attained by using SA sequences with 2×96 emissions on a 128×128 elements RC array, yielding an isotropic point spread function in the region where a constant F-number can be maintained. FWHM can be close to the diffraction limit, if the array is optimized for high quality imaging with edge apodization and a pitch of $\lambda/2$. Even the first version sub-standard arrays with λ pitch and no edge apodization can yield high quality in vivo images as shown on a rat kidney scan. Comparing these results to traditional 2-D imaging, it should be kept in mind that the $y-z$ and $x-y$ planes are never shown. These planes for traditional linear arrays with a fixed geometric focusing have very poor resolution, which at the optimal geometric focusing often is $3-5\lambda$ and away from this focus can be $10-20\lambda$ instead of the 0.6λ attained here. With the RC arrays it is, thus, possible to attain an isotropic resolution, and much better imaging with a uniform speckle pattern is possible, where any slice and orientation can be attained retrospectively after the data has been stored.

The large size of the arrays, and the use of the full aperture during reception and synthetic transmission, makes the signal-to-noise ratio high. The penetration depth is above 550λ even for low-intensity and low MI transmission, and can be increased to be above 800λ for higher pressure transmission surpassing that of conventional 1-D arrays. This is also surpassing 2-D matrix arrays, as their elements are small and often sparse arrays have to be used to keep the element count manageable.

Tensor velocity imaging can also be obtained using RC array with only 62 to 128 receiving elements and a transverse oscillation approach. The full velocity vector in any direction and at any place in the volume can be shown as a function of time. Using SA imaging and recursive imaging makes it possible to retrospectively probe any location in the volume and see the time evolution of the flow. Vortices and complex flow are easily visualized for any slice, making quantification easier. The method is complex with interleaved emissions, transverse oscillation, motion correction and dedicated beamformers and estimators resulting in a high computational load. The demands are, however, a factor 62 to 128 times lower than for a fully populated array, and modern GPUs offer thousands of processing units to make real time beamforming and estimation possible.

Volumetric super resolution imaging can also be attained by RC arrays with a resolution down to 15 μm . A long observation over minutes is essential to ensure imaging of the smallest vessels, and the data rate from the arrays should therefore be low. This is very difficult to attain for fully populated or sparse matrix arrays due to the many elements, and they are also difficult to manufacture due to the small $\lambda/2$ pitch elements, when the frequency is high. RC arrays therefore have distinct advantages for SRI as the data rate corresponds to normal linear arrays, and high frequency arrays are easier to manufacturer and attain the needed signal-to-noise ratio for the low MI emissions demanded for contrast agents. Here, synthetic aperture is also beneficial as the emitted MI is low, and a good SNR is attained, when all emissions are combined.

RC arrays currently also have a number of drawbacks. The imaging is now performed by switching between the transmitting and receiving aperture, and this necessitates more emissions for SA 3-D imaging than what is currently used for 2-D SA imaging. Often only 8 to 12 emissions are needed for very high quality 2-D SA images, whereas 48 to 96 times 2 emissions are needed for an optimal volumetric image quality. New methods for improving this are currently being investigated [47]. It should also be possible to develop combined sequences, where data is acquired for both anatomic and functional imaging with an optimal image quality at fast volume rates, and where both high and low velocities can be reliably estimated from the same data. This is an area of active research.

The contrast in 3-D imaging is also poorer than for 2-D imaging, and this should be further optimized. This problem is also related to the lack of proper arrays. Rasmussen et al. [24] showed that edge apodization of the elements is vital for avoiding ghost echoes, and the imaging also benefits from having $\lambda/2$ pitch elements, which very few RC arrays have. Having better arrays with the correct geometry will obviously improve both image quality and frame rate to mature RC technology. The imaging region of current flat arrays is also limited to the rectangular region of the transducer footprint. This can possibly be solved by employing lensed RC arrays or convex RC arrays, but again proper arrays are lacking and should be developed.

Overall it can, however, be stated that RC arrays can fulfill

all the demands for fast, high quality volumetric ultrasound imaging. Anatomic, flow, functional and super resolution imaging have all been demonstrated for simulations and phantom measurements and a few in vivo examples. It is our hope that the great potential of general row-column imaging will be demonstrated in future clinical trials using optimized arrays. The combination of having a large array capable of having a good focusing, contrast, and penetration depth can, especially for abdominal imaging, lead to high quality 3-D anatomic and functional images.

REFERENCES

- [1] R. E. Davidsen, J. A. Jensen, and S. W. Smith, "Two-dimensional random arrays for real time volumetric imaging," *Ultrason. Imaging*, vol. 16, no. 3, pp. 143–163, July 1994.
- [2] S. S. Brunke and G. R. Lockwood, "Broad-bandwidth radiation patterns of sparse two-dimensional vernier arrays," *IEEE Trans. Ultrason. Ferroelec. Freq. Contr.*, vol. 44, no. 5, pp. 1101–1109, sep 1997.
- [3] J. T. Yen and S. W. Smith, "Real-time rectilinear volumetric imaging using a periodic array," *Ultrasound in Medicine & Biology*, vol. 28, no. 7, pp. 923–931, jul 2002.
- [4] A. Austeng and S. Holm, "Sparse 2-D arrays for 3-D phased array imaging - Design methods," *IEEE Trans. Ultrason. Ferroelec. Freq. Contr.*, vol. 49, no. 8, pp. 1073–1086, 2002.
- [5] B. Diarra, M. Robini, P. Tortoli, C. Cachard, and H. Liebgott, "Design of optimal 2-D nongrid sparse arrays for medical ultrasound," *IEEE Trans. Biomed. Eng.*, vol. 60, no. 11, pp. 3093–3102, 2013.
- [6] A. Ramalli, E. Boni, E. Roux, H. Liebgott, and P. Tortoli, "Design, implementation, and medical applications of 2-D ultrasound sparse arrays," *IEEE Trans. Ultrason. Ferroelec. Freq. Contr.*, pp. 1–1, 2022.
- [7] C. E. Morton and G. R. Lockwood, "Theoretical assessment of a crossed electrode 2-D array for 3-D imaging," in *Proc. IEEE Ultrason. Symp.*, 2003, pp. 968–971.
- [8] N. M. Daher and J. T. Yen, "Rectilinear 3-D ultrasound imaging using synthetic aperture techniques," in *Proc. IEEE Ultrason. Symp.*, vol. 2, 2004, pp. 1270–1273.
- [9] —, "2-D array for 3-D ultrasound imaging using synthetic aperture techniques," *IEEE Trans. Ultrason. Ferroelec. Freq. Contr.*, vol. 53, no. 5, pp. 912–924, 2006.
- [10] C. H. Seo and J. T. Yen, "64 x 64 2-D array transducer with row-column addressing," in *Proc. IEEE Ultrason. Symp.*, vol. 1, 2006, pp. 74–77.
- [11] A. Savoia, V. Bavaro, G. Caliano, A. Caronti, R. Carotenuto, P. Gatta, C. Longo, and M. Pappalardo, "Crisscross 2D cMUT array: Beamforming strategy and synthetic 3D imaging results," *Proc. IEEE Ultrason. Symp.*, pp. 1598–1601, 2007.
- [12] C. H. Seo and J. T. Yen, "256x256 2-D array transducer with row-column addressing for 3-D imaging," in *Proc. IEEE Ultrason. Symp.*, 2007, pp. 2381–2384.
- [13] —, "Recent results using a 256 x 256 2-D array transducer for 3-D rectilinear imaging," in *Proc. IEEE Ultrason. Symp.*, vol. 1-4, 2008, pp. 1146–1149.
- [14] S. I. Awad and J. T. Yen, "3-D spatial compounding using a row-column array," *Ultrason. Imaging*, vol. 31, no. 2, pp. 120–130, 2009.
- [15] A. S. Logan, L. L. P. Wong, and J. T. W. Yeow, "2-D CMUT wafer bonded imaging arrays with a row-column addressing scheme," in *Proc. IEEE Ultrason. Symp.*, sep 2009, pp. 984–987.
- [16] C. H. Seo and J. T. Yen, "A 256 x 256 2-D array transducer with row-column addressing for 3-D rectilinear imaging," *IEEE Trans. Ultrason. Ferroelec. Freq. Contr.*, vol. 56, no. 4, pp. 837–847, April 2009.
- [17] C. E. M. Démoré, A. W. Joyce, K. Wall, and G. R. Lockwood, "Real-time volume imaging using a crossed electrode array," *IEEE Trans. Ultrason., Ferroelec., Freq. Contr.*, vol. 56, no. 6, pp. 1252–1261, 2009.
- [18] A. S. Logan, L. L. P. Wong, A. I. H. Chen, and J. T. W. Yeow, "A 32 x 32 element row-column addressed capacitive micromachined ultrasonic transducer," *IEEE Trans. Ultrason. Ferroelec. Freq. Contr.*, vol. 58, no. 6, pp. 1266–1271, June 2011.
- [19] A. I. H. Chen, L. L. P. Wong, A. S. Logan, and J. T. W. Yeow, "A CMUT-based real-time volumetric ultrasound imaging system with row-column addressing," in *Proc. IEEE Ultrason. Symp.*, oct 2011, pp. 1755–1758.
- [20] M. F. Rasmussen and J. A. Jensen, "3D ultrasound imaging performance of a row-column addressed 2D array transducer: a simulation study," in *Proc. SPIE Med. Imag.*, 2013, pp. 1–11, 86750C.
- [21] —, "3-D ultrasound imaging performance of a row-column addressed 2-D array transducer: A measurement study," in *Proc. IEEE Ultrason. Symp.*, July 2013, pp. 1460–1463.
- [22] J. T. Yen, "Beamforming of sound from two-dimensional arrays using spatial matched filters," *J. Acoust. Soc. Am.*, vol. 134, no. 5, pp. 3697–3704, 2013.
- [23] A. Sampaleanu, P. Zhang, A. Kshirsagar, W. Moussa, and R. Zemp, "Top-orthogonal-to-bottom-electrode (TOBE) CMUT arrays for 3-D ultrasound imaging," *IEEE Trans. Ultrason. Ferroelec. Freq. Contr.*, vol. 61, no. 2, pp. 266–276, 2014.
- [24] M. F. Rasmussen, T. L. Christiansen, E. V. Thomsen, and J. A. Jensen, "3-D imaging using row-column-addressed arrays with integrated apodization — Part I: Apodization design and line element beamforming," *IEEE Trans. Ultrason. Ferroelec. Freq. Contr.*, vol. 62, no. 5, pp. 947–958, 2015.
- [25] T. L. Christiansen, M. F. Rasmussen, J. P. Bagge, L. N. Moesner, J. A. Jensen, and E. V. Thomsen, "3-D imaging using row-column-addressed arrays with integrated apodization — part II: Transducer fabrication and experimental results," *IEEE Trans. Ultrason. Ferroelec. Freq. Contr.*, vol. 62, no. 5, pp. 959–971, 2015.
- [26] H. Bouzari, M. Engholm, S. I. Nikolov, M. B. Stuart, E. V. Thomsen, and J. A. Jensen, "Imaging performance for two row-column arrays," *IEEE Trans. Ultrason. Fer-*

- roelec. Freq. Contr.*, vol. 66, no. 7, pp. 1209–1221, 2019.
- [27] A. W. Joyce and G. R. Lockwood, “Crossed-array transducer for real-time 3D imaging,” in *Proc. IEEE Ultrason. Symp.*, 2014, pp. 2116–2120.
- [28] A. S. Savoia, B. Mauti, L. Fanni, G. Caliano, E. Boni, P. Mattesini, M. Scaringella, and P. Tortoli, “A 120+120-element crisscross CMUT probe with real-time switchable electronic and Fresnel focusing capabilities,” *Proc. IEEE Ultrason. Symp.*, p. 8580084, 2018.
- [29] E. Boni, L. Bassi, A. Dallai, F. Guidi, V. Meacci, A. Ramalli, S. Ricci, and P. Tortoli, “ULA-OP 256: A 256-channel open scanner for development and real-time implementation of new ultrasound methods,” *IEEE Trans. Ultrason. Ferroelec. Freq. Contr.*, vol. 63, no. 10, pp. 1488–1495, 2016.
- [30] R. J. Zemp, W. Zheng, and P. Zhang, “Feasibility of top-orthogonal-to-bottom electrode (TOBE) 2D CMUT arrays for low-channel-count 3D imaging,” in *Proc. IEEE Ultrason. Symp.*, 2011, pp. 498–502.
- [31] R. K. W. Chee, A. Sampaleanu, D. Rishi, and R. J. Zemp, “Top orthogonal to bottom electrode (TOBE) 2-D CMUT arrays for 3-D photoacoustic imaging,” *IEEE Trans. Ultrason. Ferroelec. Freq. Contr.*, vol. 61, no. 8, pp. 1393–1395, 2014.
- [32] R. K. W. Chee and R. J. Zemp, “Feasibility of modulation-encoded TOBE CMUTs for real-time 3-D imaging,” *IEEE Trans. Ultrason. Ferroelec. Freq. Contr.*, vol. 62, no. 4, pp. 771–775, 2015.
- [33] C. Ceroici, T. Harrison, and R. Zemp, “Fast orthogonal row-column electronic scanning (FORCES) with top orthogonal to bottom electrode (TOBE) arrays,” *IEEE Trans. Ultrason. Ferroelec. Freq. Contr.*, vol. 64, no. 6, pp. 1009–1014, 2017.
- [34] K. Latham, C. Ceroici, C. A. Samson, R. J. Zemp, and J. A. Brown, “Simultaneous azimuth and fresnel elevation compounding: A fast 3-D imaging technique for crossed-electrode arrays,” *IEEE Trans. Ultrason. Ferroelec. Freq. Contr.*, vol. 65, no. 9, pp. 1657–1668, 2018.
- [35] C. Ceroici, K. Latham, B. A. Greenlay, J. A. Brown, and R. J. Zemp, “Fast orthogonal row-column electronic scanning experiments and comparisons,” *IEEE Trans. Ultrason. Ferroelec. Freq. Contr.*, vol. 66, no. 6, pp. 1093–1101, 2019.
- [36] K. Latham, C. Samson, and J. Brown, “A new 3-D imaging technique integrating ultrafast compounding, Hadamard encoding, and reconfigurable Fresnel lensing,” *IEEE Trans. Ultrason. Ferroelec. Freq. Contr.*, vol. 68, no. 5, pp. 1618–1627, 2021.
- [37] M. Flesch, M. Pernot, J. Provost, G. Ferin, A. Nguyen-Dinh, M. Tanter, and T. Deffieux, “4D in vivo ultrafast ultrasound imaging using a row-column addressed matrix and coherently-compounded orthogonal plane waves,” *Phys. Med. Biol.*, vol. 62, no. 11, pp. 4571–4588, 2017.
- [38] J. Sauvage, M. Flesch, G. Ferin, A. Nguyen-Dinh, J. Poree, M. Tanter, M. Pernot, and T. Deffieux, “A large aperture row column addressed probe for in vivo 4D ultrafast Doppler ultrasound imaging,” *Phys. Med. Biol.*, vol. 63, pp. 1–12, 2018.
- [39] J. Sauvage, J. Porée, C. Rabut, G. Férin, M. Flesch, B. Rosinski, A. Nguyen-Dinh, M. Tanter, M. Pernot, and T. Deffieux, “Ultrafast 4D doppler imaging of the rat brain with a large aperture row column addressed probe,” *Proc. IEEE Ultrason. Symp.*, 2018.
- [40] —, “4D functional imaging of the rat brain using a large aperture row-column array,” *IEEE Trans. Med. Imag.*, vol. 39, no. 6, pp. 1884–1893, June 2020.
- [41] M. Engholm, H. Bouzari, T. L. Christiansen, C. Beers, J. P. Bagge, L. N. Moesner, S. E. Diederichsen, M. B. Stuart, J. A. Jensen, and E. V. Thomsen, “Probe development of CMUT and PZT row-column-addressed 2-D arrays,” *Sens. Actuators A: Phys.*, vol. 273, pp. 121–133, 2018.
- [42] M. Engholm, H. Bouzari, C. Beers, J. A. Jensen, and E. V. Thomsen, “Increasing the field-of-view of row-column-addressed ultrasound transducers: Implementation of a diverging compound lens,” *Ultrasonics*, vol. 88, pp. 97–105, 2018.
- [43] M. Engholm, C. Beers, A. S. Havreland, B. G. Tomov, J. A. Jensen, and E. V. Thomsen, “A row-column-addressed 2D probe with an integrated compound diverging lens,” in *Proc. IEEE Ultrason. Symp.*, 2018, p. 8579955.
- [44] O. T. von Ramm, S. W. Smith, and H. G. Pavy, “High speed ultrasound volumetric imaging system – Part II: Parallel processing and image display,” *IEEE Trans. Ultrason. Ferroelec. Freq. Contr.*, vol. 38, no. 2, pp. 109–115, 1991.
- [45] D. P. Shattuck, M. D. Weinschenker, S. W. Smith, and O. T. von Ramm, “Explososcan: A parallel processing technique for high speed ultrasound imaging with linear phased arrays,” *J. Acoust. Soc. Am.*, vol. 75, pp. 1273–1282, 1984.
- [46] S. W. Smith, H. G. Pavy, and O. T. von Ramm, “High speed ultrasound volumetric imaging system – Part I: Transducer design and beam steering,” *IEEE Trans. Ultrason. Ferroelec. Freq. Contr.*, vol. 38, pp. 100–108, 1991.
- [47] J. Hansen-Shearer, M. Lerendegui, M. Toulemonde, and M. X. Tang, “Ultrafast 3-D ultrasound imaging using row-column array specific frame-multiply-and-sum beamforming,” *IEEE Trans. Ultrason. Ferroelec. Freq. Contr.*, vol. 69, no. 2, pp. 480–488, 2021.
- [48] J. A. Jensen, S. Nikolov, K. L. Gammelmark, and M. H. Pedersen, “Synthetic aperture ultrasound imaging,” *Ultrasonics*, vol. 44, pp. e5–e15, 2006.
- [49] C. H. Frazier and W. D. O’Brien, “Synthetic aperture techniques with a virtual source element,” *IEEE Trans. Ultrason. Ferroelec. Freq. Contr.*, vol. 45, no. 1, pp. 196–207, 1998.
- [50] K. L. Gammelmark and J. A. Jensen, “Multielement synthetic transmit aperture imaging using temporal encoding,” *IEEE Trans. Med. Imag.*, vol. 22, no. 4, pp. 552–563, 2003.
- [51] N. Oddershede and J. A. Jensen, “Effects influencing focusing in synthetic aperture vector flow imaging,” *IEEE Trans. Ultrason. Ferroelec. Freq. Contr.*, vol. 54, no. 9,

- pp. 1811–1825, 2007.
- [52] M. L. Ommen, M. Schou, C. Beers, J. A. Jensen, N. B. Larsen, and E. V. Thomsen, “3D printed calibration micro-phantoms for super-resolution ultrasound imaging validation,” *Ultrasonics*, vol. 114, p. 106353, 2021.
- [53] J. A. Jensen and N. B. Svendsen, “Calculation of pressure fields from arbitrarily shaped, apodized, and excited ultrasound transducers,” *IEEE Trans. Ultrason. Ferroelec. Freq. Contr.*, vol. 39, no. 2, pp. 262–267, 1992.
- [54] J. A. Jensen, “Field: A program for simulating ultrasound systems,” *Med. Biol. Eng. Comp.*, vol. 10th Nordic-Baltic Conference on Biomedical Imaging, Vol. 4, Supplement 1, Part 1, pp. 351–353, 1996.
- [55] M. Schou, A. S. Havreland, M. Engholm, M. B. Stuart, E. V. Thomsen, and J. A. Jensen, “Design of a novel zig-zag 192+192 row column addressed transducer: A simulation study,” in *Proc. IEEE Ultrason. Symp.*, 2018, pp. 1–4.
- [56] J. A. Jensen, H. Holten-Lund, R. T. Nilsson, M. Hansen, U. D. Larsen, R. P. Domsten, B. G. Tomov, M. B. Stuart, S. I. Nikolov, M. J. Pihl, Y. Du, J. H. Rasmussen, and M. F. Rasmussen, “SARUS: A synthetic aperture real-time ultrasound system,” *IEEE Trans. Ultrason. Ferroelec. Freq. Contr.*, vol. 60, no. 9, pp. 1838–1852, 2013.
- [57] FDA, “Information for manufacturers seeking marketing clearance of diagnostic ultrasound systems and transducers,” Center for Devices and Radiological Health, United States Food and Drug Administration, Tech. Rep., 2008.
- [58] M. B. Stuart, P. M. Jensen, J. T. R. Olsen, A. B. Kristensen, M. Schou, B. Dammann, H. H. B. Sørensen, and J. A. Jensen, “Real-time volumetric synthetic aperture software beamforming of row-column probe data,” *IEEE Trans. Ultrason. Ferroelec. Freq. Contr.*, vol. 68, no. 8, pp. 2608–2618, 2021.
- [59] M. B. Stuart, M. Schou, and J. A. Jensen, “Row-column beamforming with dynamic apodizations on a GPU,” in *Proc. SPIE Med. Imag.*, 2019, p. 109550Q, paper number 10955-20.
- [60] H. Bouzari, M. Engholm, C. Beers, M. B. Stuart, S. I. Nikolov, E. V. Thomsen, and J. A. Jensen, “Curvilinear 3-D imaging using row-column-addressed 2-D arrays with a diverging lens: Feasibility study,” *IEEE Trans. Ultrason. Ferroelec. Freq. Contr.*, vol. 64, no. 99, pp. 978–988, 2017.
- [61] H. Bouzari, M. Engholm, C. Beers, S. I. Nikolov, M. B. Stuart, E. V. Thomsen, and J. A. Jensen, “Curvilinear 3-D imaging using row-column addressed 2-D arrays with a diverging lens: Phantom study,” *IEEE Trans. Ultrason. Ferroelec. Freq. Contr.*, vol. 65, no. 7, pp. 1182–1192, 2018.
- [62] S. H. Øygard, M. Audoin, A. Austeng, E. V. Thomsen, M. B. Stuart, and J. A. Jensen, “Accurate prediction of transmission through a lensed row-column addressed array,” *J. Acoust. Soc. Am.*, vol. 151, no. 5, pp. 3207–3218, 2022.
- [63] J. A. Jensen, *Estimation of Blood Velocities Using Ultrasound: A Signal Processing Approach*. New York: Cambridge University Press, 1996.
- [64] J. A. Jensen, S. I. Nikolov, A. Yu, and D. Garcia, “Ultrasound vector flow imaging I: Sequential systems,” *IEEE Trans. Ultrason. Ferroelec. Freq. Contr.*, vol. 63, no. 11, pp. 1704–1721, 2016.
- [65] —, “Ultrasound vector flow imaging II: Parallel systems,” *IEEE Trans. Ultrason. Ferroelec. Freq. Contr.*, vol. 63, no. 11, pp. 1722–1732, 2016.
- [66] J. A. Jensen and P. Munk, “A new method for estimation of velocity vectors,” *IEEE Trans. Ultrason. Ferroelec. Freq. Contr.*, vol. 45, no. 3, pp. 837–851, 1998.
- [67] J. A. Jensen, “A new estimator for vector velocity estimation,” *IEEE Trans. Ultrason. Ferroelec. Freq. Contr.*, vol. 48, no. 4, pp. 886–894, 2001.
- [68] A. H. Brandt, R. Moshavegh, K. L. Hansen, L. Lonn, J. A. Jensen, and M. Nielsen, “Vector flow imaging compared with pulse wave Doppler for estimation of peak velocity in the portal vein,” *Ultrasound Med. Biol.*, vol. 44, no. 3, pp. 593–601, 2018.
- [69] S. Holbek, T. L. Christiansen, M. B. Stuart, C. Beers, E. V. Thomsen, and J. A. Jensen, “3-D vector flow estimation with row-column addressed arrays,” *IEEE Trans. Ultrason. Ferroelec. Freq. Contr.*, vol. 63, no. 11, pp. 1799–1814, 2016.
- [70] S. Holbek, K. H. Lindskov, H. Bouzari, C. Ewertsen, M. B. Stuart, C. Thomsen, M. B. Nielsen, and J. A. Jensen, “Common carotid artery flow measured by 3-D ultrasonic vector flow imaging and validated with magnetic resonance imaging,” *Ultrasound Med. Biol.*, vol. 43, no. 10, pp. 2213–2220, 2017.
- [71] M. Schou, L. T. Jørgensen, C. Beers, M. S. Traberg, B. G. Tomov, M. B. Stuart, and J. A. Jensen, “Fast 3-D velocity estimation in 4-D using a 62 + 62 row-column addressed array,” *IEEE Trans. Ultrason. Ferroelec. Freq. Contr.*, vol. 68, no. 3, pp. 608–623, 2020.
- [72] L. T. Jørgensen, M. Schou, M. B. Stuart, and J. A. Jensen, “Tensor velocity imaging with motion correction,” *IEEE Trans. Ultrason. Ferroelec. Freq. Contr.*, vol. 68, no. 5, pp. 1676–1686, 2020.
- [73] J. A. Jensen, “Estimation of high velocities in synthetic aperture imaging: I: Theory,” *IEEE Trans. Ultrason. Ferroelec. Freq. Contr.*, vol. 66, no. 6, pp. 1024–1031, 2019.
- [74] —, “Estimation of high velocities in synthetic aperture imaging: II: Experimental investigation,” *IEEE Trans. Ultrason. Ferroelec. Freq. Contr.*, vol. 66, no. 6, pp. 1032–1038, 2019.
- [75] L. T. Jørgensen, M. S. Traberg, M. B. Stuart, and J. A. Jensen, “Performance assessment of row-column transverse oscillation tensor velocity imaging using computational fluid dynamics simulation of carotid bifurcation flow,” *IEEE Trans. Ultrason. Ferroelec. Freq. Contr.*, vol. 69, no. 4, pp. 1230–1242, 2022.
- [76] O. M. Viessmann, R. J. Eckersley, K. Christensen-Jeffries, M. X. Tang, and C. Dunsby, “Acoustic super-resolution with ultrasound and microbubbles,” *Phys. Med. Biol.*, vol. 58, pp. 6447–6458, 2013.
- [77] M. A. O’Reilly and K. Hynynen, “A super-resolution ultrasound method for brain vascular mapping,” *Med.*

- Phys.*, vol. 40, no. 11, pp. 110 701–7, 2013.
- [78] Y. Desailly, J. Pierre, O. Couture, and M. Tanter, “Resolution limits of ultrafast ultrasound localization microscopy,” *Phys. Med. Biol.*, vol. 60, no. 22, pp. 8723–8740, 2015.
- [79] K. Christensen-Jeffries, R. J. Browning, M. Tang, C. Dunsby, and R. J. Eckersley, “In vivo acoustic super-resolution and super-resolved velocity mapping using microbubbles,” *IEEE Trans. Med. Imag.*, vol. 34, no. 2, pp. 433–440, 2015.
- [80] C. Errico, J. Pierre, S. Pezet, Y. Desailly, Z. Lenkei, O. Couture, and M. Tanter, “Ultrafast ultrasound localization microscopy for deep super-resolution vascular imaging,” *Nature*, vol. 527, pp. 499–502, 2015.
- [81] D. Ackermann and G. Schmitz, “Detection and tracking of multiple microbubbles in ultrasound B-mode images,” *IEEE Trans. Ultrason. Ferroelec. Freq. Contr.*, vol. 63, no. 1, pp. 72–82, 2016.
- [82] K. Christensen-Jeffries, O. Couture, P. A. Dayton, Y. C. Eldar, K. Hynynen, F. Kiessling, M. O’Reilly, G. F. Pinton, G. Schmitz, M. Tang *et al.*, “Super-resolution ultrasound imaging,” *Ultrasound Med. Biol.*, vol. 46, no. 4, pp. 865–891, 2020.
- [83] K. B. Hansen, C. A. Villagomez-Hoyos, J. Brasen, K. Diamantis, V. Sboros, C. M. Sørensen, and J. A. Jensen, “Robust microbubble tracking for super resolution imaging in ultrasound,” in *Proc. IEEE Ultrason. Symp.*, 2016, pp. 1–4.
- [84] J. Foiret, H. Zhang, T. Ilovitsh, L. Mahakian, S. Tam, and K. W. Ferrara, “Ultrasound localization microscopy to image and assess microvasculature in a rat kidney,” *Scientific Reports*, vol. 7, no. 1, pp. 13 662:1–12, 2017.
- [85] V. Hingot, C. Errico, M. Tanter, and O. Couture, “Sub-wavelength motion-correction for ultrafast ultrasound localization microscopy,” *Ultrasonics*, vol. 77, pp. 17–21, 2017.
- [86] S. Harput, K. Christensen-Jeffries, J. Brown, Y. Li, K. J. Williams, A. H. Davies, R. J. Eckersley, C. Dunsby, and M. Tang, “Two-stage motion correction for super-resolution ultrasound imaging in human lower limb,” *IEEE Trans. Ultrason. Ferroelec. Freq. Contr.*, vol. 65, no. 5, pp. 803–814, 2018.
- [87] M. Piepenbrock, S. Dencks, and G. Schmitz, “Reliable motion estimation in super-resolution US by reducing the interference of microbubble movement,” *Proc. IEEE Ultrason. Symp.*, vol. 2019, p. 8925566, 2019.
- [88] T. M. Kierski, D. Espindola, I. G. Newsome, E. Cherin, J. Yin, F. S. Foster, C. E. M. Demore, G. F. Pinton, and P. A. Dayton, “Superharmonic ultrasound for motion-independent localization microscopy: Applications to microvascular imaging from low to high flow rates,” *IEEE Trans. Ultrason. Ferroelec. Freq. Contr.*, vol. 67, no. 5, pp. 957–967, 2020.
- [89] I. Taghavi, S. B. Andersen, C. A. V. Hoyos, M. B. Nielsen, C. M. Sørensen, and J. A. Jensen, “In vivo motion correction in super resolution imaging of rat kidneys,” *IEEE Trans. Ultrason. Ferroelec. Freq. Contr.*, vol. 68, no. 10, pp. 3082–3093, 2021.
- [90] J. A. Jensen, M. L. Ommen, S. H. Øygaard, M. Schou, T. Sams, M. B. Stuart, C. Beers, E. V. Thomsen, N. B. Larsen, and B. G. Tomov, “Three-dimensional super resolution imaging using a row-column array,” *IEEE Trans. Ultrason. Ferroelec. Freq. Contr.*, vol. 67, no. 3, pp. 538–546, 2020.
- [91] S. I. Nikolov, K. Gammelmark, and J. A. Jensen, “Recur-sive ultrasound imaging,” in *Proc. IEEE Ultrason. Symp.*, vol. 2, 1999, pp. 1621–1625.
- [92] I. Taghavi, S. B. Andersen, S. B. Sjøgaard, M. B. Nielsen, C. M. Sørensen, M. B. Stuart, and J. A. Jensen, “Auto-matic classification of arterial and venous flow in super-resolution ultrasound images of rat kidneys,” in *Proc. IEEE Ultrason. Symp.*, 2021, pp. 1–4.
- [93] S. B. Andersen, I. Taghavi, H. M. Kjer, S. B. Sjøgaard, C. Gundlach, V. A. Dahl, M. B. Nielsen, A. B. Dahl, J. A. Jensen, and C. M. Sørensen, “Evaluation of 2D super-resolution ultrasound imaging of the rat renal vasculature using ex vivo micro-computed tomography,” *Scientific Reports*, vol. 11, no. 1, p. 24335, 2021.



Jørgen Arendt Jensen (M’93-SM’02-F’12) received the MSc degree in 1985, the Ph.D. degree in 1989, and the Dr.Techn. degree all from the university in 1996. Since 1993, he has been a Full Professor of Biomedical Signal Processing with the Department of Electrical Engineering, Technical University of Denmark. He has been the founder and head of the Center for Fast Ultrasound Imaging since its inauguration in 1998. CFU has contributed with innovations in transverse oscillation vector flow imaging, synthetic aperture flow imaging in 2D and 3D, ultrasound simulation, research scanners, and row-column probes and beamforming. He has published more than 500 journal and conference papers on signal processing and medical ultrasound and the book *Estimation of Blood Velocities Using Ultrasound* (Cambridge Univ. Press), 1996. He is also the developer and maintainer of the Field II simulation program. He has been a visiting scientist at Duke University, Stanford University, and the University of Illinois at Urbana-Champaign. He was founder and head of the Biomedical Engineering group from 2007 to 2010. In 2003, he was one of the founders of the biomedical engineering program in Medicine and Technology, which is a joint degree program between the Technical University of Denmark and the Faculty of Health and Medical Sciences at the University of Copenhagen. The degree is one of the most sought-after engineering degrees in Denmark. He was chairman of the study board from 2003 to 2010 and Adjunct Professor with the University of Copenhagen from 2005 to 2010. He has given a number of short courses on simulation, synthetic aperture imaging, and flow estimation at international scientific conferences and teaches biomedical signal processing and medical imaging at the Technical University of Denmark. His research is centered around simulation of ultrasound imaging, synthetic aperture imaging, super resolution imaging, vector blood flow estimation, 3D imaging, row-column probes, and construction of ultrasound research systems. Dr. Jensen has given more than 60 invited talks at international meetings and received several awards for his research, most recently the Grand Solutions Prize from the Danish Minister of Science, the order of the Dannebrog by her Majesty the Queen of Denmark, and the 2019 Rayleigh award by the IEEE UFFC society.



Mikkel Schou received the M.Sc. degree in biomedical engineering from the Technical University of Denmark, Kongens Lyngby, Denmark, and the University of Copenhagen, Copenhagen, Denmark, in 2017. He is currently pursuing a Ph.D. degree in biomedical engineering with the Center for Fast Ultrasound Imaging, Technical University of Denmark. The topic of his Ph.D. research is 3-D ultrasound perfusion and flow imaging using row-column arrays.



Iman Taghavi obtained his PhD degree on ultrasound super resolution imaging at the Technical University of Denmark in 2022. He is currently affiliated with the Center for fast Ultrasound Imaging at DTU as a postdoc specialising in super resolution imaging.



Lasse Thurm Jørgensen received the M.Sc. Degree in biomedical engineering from the Technical University of Denmark, Lyngby, Denmark, in 2019. He is currently a Ph.D. candidate at DTU Health Tech in the Center for Fast Ultrasound imaging, where his topic of research includes motion estimation with 3-D ultrasound systems.



Sigrid Huesebø Øygaard obtained her PhD degree on ultrasound row-column imaging at the Technical University of Denmark in 2022. She is currently affiliated with the company Dolphitech in Norway.



Borislav G. Tomov received the M.Sc. degree in electronics engineering from the Technical University of Sofia, Sofia, Bulgaria, in 1996, and the Ph.D. degree in medical electronics from the Technical University of Denmark, Kongens Lyngby, Denmark, in 2003. He is currently a Senior Researcher with Center for Fast Ultrasound Imaging, Department of Health Technology, Technical University of Denmark. His research interests include medical ultrasound signal processing and ultrasound scanner architectures and implementations.



scatter phantoms.

Martin Lind Ommen received the M.Sc. degree in physics and nanotechnology from the Technical University of Denmark, Lyngby, Denmark, in 2017, where he is currently pursuing the Ph.D. degree with the Biomedical Engineering Section, Department of Health Technology. His current research interests include microfabrication and nanofabrication in general, in particular the fabrication of capacitive micromachined ultrasonic transducers (CMUTs), as well as phantom fabrication, with a current focus on stereolithographic fabrication of microflow and



Matthias Bo Stuart received the M.Sc. and Ph.D. degrees in Computer Engineering from the Technical University of Denmark, Lyngby, Denmark, in 2006 and 2010, respectively. He is currently an Associate Professor with the Biomedical Engineering Section, Department of Health Technology at the Technical University of Denmark. His research interests include synthetic aperture methods for both anatomical and flow imaging in both 2-D and 3-D, ultrasound systems, and real-time implementations of ultrasound processing algorithms.



Kitty Steenberg obtained her B.Sc. and M.Sc. degrees in physics and nanotechnology engineering from the Technical University of Denmark (DTU), Kgs. Lyngby, Denmark, in 2017 and 2019, respectively. She is currently affiliated with the department of Health Tech as a Ph.D. student at DTU developing capacitive micromachined ultrasonic transducers for three-dimensional imaging. Her main interest is fabrication of microstructures.



and disease. The simulation models are also used for evaluation of the precision and accuracy of new imaging technology like 3D vector flow imaging and blood pressure estimation.

Marie Sand Traberg (Member, IEEE) is associate professor at DTU Health Technology. She received her M.Sc. degree in biomedical engineering from DTU in 2008, and in January 2012 she earned her PhD degree from there as well. In her research she combines computational biomechanics, advanced 2D and 3D imaging methods, and state-of-the-art ultrasound techniques for quantification of blood flow and soft tissue motion. This is applied in patient-specific finite element based models to gain more knowledge of cardiovascular biomechanics in health



state electronics, microtechnology, and nanofabrication and microfabrication. His current research interests include all aspects of capacitive micromachined ultrasonic transducers (CMUTs), general MEMS technology, and piezoelectric MEMS. Dr. Thomsen received the Danish National Advanced Technology Foundation's Grand Solution Prize in 2017, the AEG Electron Prize in 1995, and several teaching awards at DTU.

Erik Vilain Thomsen was born in Aarhus, Denmark, in 1964. He received the M.Sc. degree in physics from the University of Southern Denmark, Odense, Denmark, in 1992, and the Ph.D. degree in electrical engineering from the Technical University of Denmark (DTU), Lyngby, Denmark, in 1998. He is currently Professor with the Department of Health Technology, DTU, where he is also the Head of the MEMS Applied Sensors Group and Head of Division with responsibility for the educations in healthcare engineering. He teaches classes in solid-

PLACE
PHOTO
HERE

Nathalie Sarup Panduro is a PhD student at the Department of Biomedical Sciences at the University of Copenhagen and with the Department of Radiology, Rigshospitalet, Copenhagen.



Michael Bachmann Nielsen Michael Bachmann Nielsen is a Medical graduate from the Faculty of Health Science, University of Copenhagen, Copenhagen, Denmark, in 1985, and received the Ph.D. degree in 1994, and the Dr.Med. Dissertation degree in 1998. He is a Full Professor of Oncoradiology with the University of Copenhagen, and a Consultant with the Department of Radiology, Rigshospitalet, Copenhagen. He has authored over 275 peer-reviewed journal articles on ultrasound or radiology. His current research interests include clinical testing

of new ultrasound techniques, tumor vascularity, ultrasound elastography, training in ultrasound and artificial intelligence.



Charlotte Mehlin Sørensen received her B.Sc. in Biology from University of Copenhagen, Denmark in 1996. In 1999, she received her M.Sc. in Human Biology. She completed her PhD in Renal Physiology in 2004 and continued as Assistant Professor at UCPH until 2006 where she joined the medical company Zealand Pharma as a drug discovery scientist focusing on acute kidney injury. She returned to UCPH in 2007 and became Associate Professor in Renal Physiology in 2011. Her research focuses on renal hemodynamics and the interplay between

the renal autoregulatory mechanisms and the topology of the renal vascular tree and includes the regulatory roles of gap junctions, potassium channels and incretin hormones.